

Continuous nonlinear adaptive experimental design with gradient flow

Ruhui Jin ^{*†} Qin Li ^{*†} Stephen O. Musmann [‡] Stephen J. Wright ^{§†}

Abstract

Identifying valuable measurements is one of the main challenges in computational inverse problems, often framed as the optimal experimental design (OED) problem. In this paper, we investigate nonlinear OED within a continuously-indexed design space. This is in contrast to the traditional approaches on selecting experiments from a finite measurement set. This formulation better reflects practical scenarios where measurements are taken continuously across spatial or temporal domains. However, optimizing over a continuously-indexed space introduces computational challenges. To address these, we employ gradient-flow and optimal transport techniques, complemented by adaptive strategy for interactive optimization. Numerical results on the Lorenz 63 system and Schrödinger equation demonstrate that our solver identifies valuable measurements and achieves improved reconstruction of unknown parameters in inverse problems.

Keywords— Experimental design, nonlinear model, continuous design space, Wasserstein gradient flow, adaptive algorithm.

1 Introduction

Often in physical sciences, measurements are taken to infer unknown parameters. Typically an optimization formulation is deployed to conduct the parameter reconstruction [54, 30]. In a generic setting, the optimization is given as:

$$\boldsymbol{\sigma}^* := \arg \min_{\boldsymbol{\sigma} \in \mathbb{R}^d} \text{Loss}[\boldsymbol{\sigma}; \rho] \equiv \int_{\Omega} (\mathcal{M}(\theta; \boldsymbol{\sigma}) - \text{data}(\theta))^2 \rho(\theta) \, d\theta, \quad (1)$$

where $\boldsymbol{\sigma} \in \mathbb{R}^d$ is the unknown parameter to be recovered. The notation θ is the design variable from the design space Ω that includes all possible experimental designs. Here by design variable, we mean a set of parameters used to describe the configuration of the experiment, for instance source and detector locations and observation time. Often this design variable θ is continuously indexed, as usually seen in regression models [40, 38] and medical imaging [41, 45]. ρ is a probability measure over Ω and guides to select experiments. Empirically more measurements are selected for variable of θ when $\rho(\theta)$ is large. The system’s Parameter-to-Output (PtO) map is \mathcal{M} , meaning $\mathcal{M}(\theta; \boldsymbol{\sigma})$ gives the output at measurement index $\theta \in \Omega$ when the system is parameterized by $\boldsymbol{\sigma} \in \mathbb{R}^d$.

*Department of Mathematics, University of Wisconsin-Madison

†Institute for Foundations of Data Science, University of Wisconsin-Madison

‡School of Computer Science (SCS), Georgia Institute of Technology

§Department of Computer Sciences, University of Wisconsin-Madison

Here we specify that the mapping $\mathcal{M}(\theta; \boldsymbol{\sigma})$ itself contains no noise. Correspondingly, $\text{data}(\theta)$ is the experiment measurement at $\theta \in \Omega$ generated via ground-truth parameters $\boldsymbol{\sigma}_{\text{true}}$ with additive random noise ϵ , i.e. $\text{data}(\theta) = \mathcal{M}(\theta; \boldsymbol{\sigma}_{\text{true}}) + \epsilon$.

When the design measure ρ is fixed, the optimization formulation (1) returns an optimizer $\boldsymbol{\sigma}^*$ that finds the smallest mismatch between the generated output and the real data, and thus $\boldsymbol{\sigma}^*$ is regarded as a good approximation to the ground-truth parameter. Generally speaking, the reconstruction quality can depend on the choice of ρ . Considering the number of experimental data and field measurements are expensive or time-consuming to collect, it is specially crucial to design a ρ that reveals the importance of measurements. In this paper, we develop the efficient solver to find the optimal design ρ so to have a high quality reconstruction of $\boldsymbol{\sigma}^*$ with low cost. This problem falls into the category of optimal experimental design (OED) [6, 48, 32], which has broad applications in clinical [29, 12], engineering [12] and other natural sciences. OED provides optimality criterion to characterize the best ρ , such as A-optimality and D-optimality [39]. We study:

What data measurements are the most useful for the reconstruction?

A unique feature of the problem studied in this paper is that we allow our design variable θ to be continuously-indexed so that the design space Ω can represent objects such as spatial, temporal or angular coordinates. As a consequence, Ω is a set of uncountable many configurations. This is significantly different from the classical setting, where $|\Omega| < \infty$ and thus ρ can be numerically represented by a finite-dimensional vector. This change calls for a new formulation over \mathbf{Pr}_2 (2) supported on a continuous domain Ω :

$$\mathbf{Pr}_2(\Omega) = \left\{ \rho \mid \rho(\theta) \geq 0, \forall \theta \in \Omega, \int_{\Omega} \rho(\theta) d\theta = 1, \int_{\Omega} |\theta|^2 \rho(\theta) d\theta < \infty \right\}. \quad (2)$$

We now summarize our formulation. We are to solve a two-level optimization problem, with the outer layer on $\rho \in \mathbf{Pr}_2(\Omega)$, and inner layer on $\boldsymbol{\sigma}$.

$$\rho^{\text{opt}} := \arg \min_{\rho \in \mathbf{Pr}_2(\Omega)} F[\rho; \boldsymbol{\sigma}^*[\rho]], \quad \text{with } \boldsymbol{\sigma}^*[\rho] \text{ being the optimum of (1)}. \quad (3)$$

Here the functional F is a certain criterion that quantifies the experimental design quality. According to the formulation (3), for every design measure ρ , one can find its associated best reconstruction of $\boldsymbol{\sigma}^*[\rho]$ by solving the optimization problem (1). We then look for the best ρ^{opt} in $\mathbf{Pr}_2(\Omega)$ (2) that minimizes the criterion F in (3).

In various settings, the OED criterion F is chosen according to a specific pursuit. To be general, in this paper, we follow the classical OED criteria such as the A- and D-optimal designs [39], both of which are to examine the property of the Hessian matrix of the loss function (1). Heuristically speaking, better-conditioned Hessian leads to more stable reconstruction against measurement error, due to the local strong convexity of the optimization (1). Applying the same intuition here, F also takes on the form that evaluates Hessian's spectrum.

To proceed with (3), we encounter two immediate difficulties:

- Solving an optimization problem over \mathbf{Pr}_2 . The outer loop in (3) is an optimization posed over the probability measure space \mathbf{Pr}_2 with continuous Ω . Since $\mathbf{Pr}_2(\Omega)$ is an infinite-dimensional function space, there is not a general numerical representation, so standard implementations of gradient descent on Euclidean or Sobolev spaces are not possible here. A modified gradient based optimization solver over \mathbf{Pr}_2 thus needs to be incorporated.

- The convoluted OED formulation in (3). This two-layer complication of ρ and $\sigma^*[\rho]$ occurs when the PtO map \mathcal{M} is nonlinear, raising the computation complexity dramatically. Indeed, in a brute-force computation, in each outer-loop update, the inner loop σ^* has to be updated accordingly, and solving (1) can be costly. Hence we are to develop a solver that avoids repeatedly computing the inner loop optimization.

Fortunately, over the past few years, significant progress has been made in the domain of optimal transport [21] and gradient flow [50]. Techniques over optimizing \mathbf{Pr}_2 (2) have been developed and made easy to use. Our problem (3) can see benefit from their direct applications. Moreover, applying the implicit function theorem, we can translate the dynamics of ρ to that of $\sigma^*[\rho]$. This removes the procedure of exhaustively solving the inner-loop optimization for σ^* . These two strategies combined provide us an efficient two-layer optimization solver to the design (3).

By no means are we the first group examining the optimal design problem. We take an overview of the rich related works in the following subsection and describe our contribution next. Our method combines the classical optimal design and the novel gradient flow technique. We briefly discuss them in Section 2. Section 3 contains this work’s new developments, where we propose the explicit formulation for the nonlinear experimental design (3). Further we present the brute-force computational method, and the relaxed solver through implicit functional theorem. Numerical tests are presented respectively in Section 4 and Section 5 for the Lorenz 63 system and the Schrödinger model.

1.1 Related works

The optimal design area has developed over a long history. In the last century, OED research came into shape when rigorous statistical formulations for the design criteria were proposed and analyzed. We refer to the review articles and books [49, 48, 20, 32]. The majority of works tackle the finite design space $\Omega = \{\theta_i\}_{i=1}^m$ and calculate the optimal discrete importances $\rho(\theta_i)$ assigned to each data, hence the inference has a weighted evaluation:

$$\sigma^* := \arg \min_{\sigma \in \mathbb{R}^d} \sum_{i=1}^m \rho(\theta_i) (\mathcal{M}(\theta_i; \sigma) - \text{data}(\theta_i))^2. \quad (4)$$

The theoretical foundations [39] and combinatorial design algorithms were accomplished in this early era, such as in [9, 55, 46], among others.

Modern computing power has led to significant progress in the Bayesian inverse problems and uncertainty quantification [14, 17, 16], where the PtO map \mathcal{M} is governed by ordinary or partial differential equations [19, 1] and Bayesian formulation provides a systematic way to quantify information. In particular, OED for linear models has been thoroughly studied. This is a special case that the design quantity (3) is fixed and stays independent from the parameters σ . Classical optimization approaches combined with sparsity control [26, 28, 2] are effectively applied to the discrete weights computation. Further, stochastic optimization [36], randomized algorithms [8, 4] and surrogate modeling are deployed to enhance the computation speed. But none of these techniques work for the design scenario when Ω is continuously indexed. Note in the recent paper [37], the authors took a different view and addressed continuous OED, employing the Wasserstein gradient flow method.

However working on nonlinear OED problems [18] introduces new challenges than in the linear case. Because there is no close-form expression available to define the design criteria. Hence new

approaches are adapted in several ways, for instance deploying bilevel constrained optimizations [11, 27]; and proposing information-theoretic formulations by sequential approaches [33, 35, 22, 51, 43]; and using average Bayesian formulation without prior knowledge, such as in [3]. However, very few papers [34] are able to deal with nonlinear designs for continuously indexed Ω .

In the machine learning community, active learning (AL) [53] often goes hand in hand with experimental design. AL attempts to collect effective training data while interacting with the learning progress, as most learning problems are highly convoluted like deep neural networks [23, 52] and control problems [10]. Experimental design serves as a statistical criterion that guides AL to query data. For instance, pool-based AL augments the labelled data greedily with a new label at each iteration, making the algorithm converge to the learning goal faster and with a smaller sample complexity. Crucial analytical guarantees [15, 13, 47] and empirical advancements [7] are established in AL. Bayesian active learning and adaptive design are also established such as in [31, 24].

1.2 Our contributions

The main contribution of this manuscript is developing the computational scheme for continuous nonlinear optimal design. To the best of our knowledge, this is the first work that pursues nonlinear OED via optimizing a continuous design distribution $\rho \in \mathbf{Pr}_2(\Omega)$. We work on the two-layer algorithm framework, which alternately optimizes the continuous design measure ρ and the inference parameters σ . Crucial techniques include the gradient flow with Monte-Carlo particle method to simulate the design measure ρ , facilitating the search of measurements that carry the most information volume. With fixed experiment budget, we are to efficiently allocate the measurement to the most valuable design variables to realize parameter reconstruction σ^* . Depending on the local optimization property, we have both the brute-force and the relaxed one-step update options for solving σ^* . The two strategies are Algorithm 1 presented in Section 3.2 and Algorithm 2 in Section 3.3. To some extent, the current work is the nonlinear extension to the existing paper [37] that focused on continuous linear OED problems. The nonlinear design adds one more layer of optimization for σ^* (1).

We provide comprehensive numerical experiments of the proposed Algorithm 1 and Algorithm 2 on various nonlinear inverse problem models, including the Lorenz 63 dynamical system [44] and the steady-state Schrödinger equation [56]. The empirical performances showcase the applicability of both algorithms. In particular, the adaptive algorithms are able to achieve the best statistical design criteria and also facilitate solving the parameter successfully. Meanwhile the solved design measures reveal interesting patterns of valuable experiments that correspond to the underlying features within the physical systems.

2 Preliminaries

Two main techniques involved in our works are the classical optimal design (A- and D- optimal design in particular) and the Wasserstein gradient flow. We review them here briefly.

2.1 Optimal design for linear models

Optimal design has been extensively studied, and in the linear setting, it is often formulated via a data matrix. And the OED goal comes down to selecting matrix rows (constraints) that are most

reflective of the solution features. In particular the linear model is:

$$\mathcal{M}(\theta, \boldsymbol{\sigma}) = \mathbf{A}(\theta, :) \boldsymbol{\sigma}, \quad (5)$$

where the matrix \mathbf{A} can potentially have infinite sometimes uncountably many rows, especially when the index θ is continuously valued. The task here is to select subsets of rows in \mathbf{A} for the linear inversion of $\boldsymbol{\sigma}$.

Consider the unknowns $\boldsymbol{\sigma} \in \mathbb{R}^d$ and a design measure $\rho \in \mathbf{Pr}_2(\Omega)$. Similar to (4), suppose we reweight the experiment $\mathbf{A}(\theta, :)$ with the density $\rho(\theta)$, the reconstruction problem (1) $\min_{\boldsymbol{\sigma} \in \mathbb{R}^d} \int_{\Omega} (\mathbf{A}(\theta, :) \boldsymbol{\sigma} - \text{data}(\theta))^2 \rho(\theta) d\theta$ has an explicit analytical solution:

$$\boldsymbol{\sigma}^* = (\mathbf{A}^\top \mathbf{A}[\rho])^{-1} \cdot (\mathbf{A}^\top \text{data}[\rho]), \quad (6)$$

where

$$\begin{cases} \mathbf{A}^\top \mathbf{A}[\rho] = \int_{\Omega} \mathbf{A}(\theta, :)^{\top} \mathbf{A}(\theta, :) \rho(\theta) d\theta \in \mathbb{R}^{d \times d}, \\ \mathbf{A}^\top \text{data}[\rho] = \int_{\Omega} \mathbf{A}(\theta, :)^{\top} \text{data}(\theta) \rho(\theta) d\theta \in \mathbb{R}^d. \end{cases}$$

Since both $\mathbf{A}^\top \mathbf{A}[\rho]$ and $\mathbf{A}^\top \text{data}[\rho]$ are written in the form of expectation, numerically one can employ Monte-Carlo sampling for computation.

The uncertainties in data is amplified by the matrix inversion $(\mathbf{A}^\top \mathbf{A}[\rho])^{-1}$. In particular due to $\text{data}(\theta) = \mathbf{A}(\theta, :) \boldsymbol{\sigma}_{\text{true}} + \epsilon$ and the random Gaussian noise $\epsilon \sim \mathcal{N}(0, \delta^2)$, we have the Gaussian variable $\text{data}(\theta) \sim \mathcal{N}(\mathbf{A}(\theta, :) \boldsymbol{\sigma}_{\text{true}}, \delta^2)$ for all θ , and the reconstructed $\boldsymbol{\sigma}^*$ via (6) is also a Gaussian random variable with a modified covariance $\boldsymbol{\sigma}^* \sim \mathcal{N}(\boldsymbol{\sigma}_{\text{true}}, \delta^2 (\mathbf{A}^\top \mathbf{A}[\rho])^{-1})$. As a consequence, to minimize the sensitivity to the perturbation seen in data, it is crucial to adjust $\rho \in \mathbf{Pr}_2(\Omega)$ for a small $(\mathbf{A}^\top \mathbf{A}[\rho])^{-1}$. A-optimal and D-optimal designs are the two OED criteria used to address this design problem, evaluating how small $(\mathbf{A}^\top \mathbf{A}[\rho])^{-1}$ is. In particular, they are to optimize the trace and determinant of the variance matrix respectively, namely A-optimal looks for:

$$\rho^A := \arg \min_{\rho \in \mathbf{Pr}_2(\Omega)} F^A[\rho] \equiv \text{Tr} \left((\mathbf{A}^\top \mathbf{A}[\rho])^{-1} \right), \quad (7)$$

and D-optimal looks for:

$$\rho^D := \arg \max_{\rho \in \mathbf{Pr}_2(\Omega)} F^D[\rho] \equiv \log \left(\text{Det}(\mathbf{A}^\top \mathbf{A}[\rho]) \right). \quad (8)$$

Details are discussed in Section 3.1 in [37].

We should emphasize that the discussion above is purely for the linear problem (5). Our focus of the paper, however, is to look for its counterpart for a nonlinear map \mathcal{M} . To borrow the technique, we note that $\mathbf{A}(\theta, :) \equiv \nabla_{\boldsymbol{\sigma}} \mathcal{M}(\theta, \boldsymbol{\sigma})$ if \mathcal{M} happens to be reduced to a linear form, and thus $\mathbf{A}^\top \mathbf{A}[\rho]$ can be viewed as the Gauss-Newton Hessian matrix. As a consequence, in our formulation for the nonlinear problems, this Gauss-Newton matrix will be deployed as an analogue of $\mathbf{A}^\top \mathbf{A}[\rho]$ in linear A-, D-optimal designs.

2.2 Gradient flow and particle method

Next we discuss the optimization technique over \mathbf{Pr}_2 (2). As seen in (3), the OED problem is a constrained optimization that is formulated over a probability measure space $\mathbf{Pr}_2(\Omega)$. To run this optimization calls for a numerical strategy that honors the probability manifold $\mathbf{Pr}_2(\Omega)$ geometry.

Given an objective functional:

$$\min_{\rho \in \mathbf{Pr}_2(\Omega)} F[\rho],$$

running gradient descent for this objective functional demands a proper definition of the “gradient”. To do so, note that the probability measure space is nonlinear, and is typically equipped with the Wasserstein metric, the vanilla gradient descent has to be accordingly adjusted.

We follow the standard definition for the Wasserstein-2 distance:

$$W_2(\mu, \nu) = \inf_{\gamma \in \Gamma(\mu, \nu)} \left(\int_{\Omega \times \Omega} \|x - y\|_2^2 d\gamma(x, y) \right)^{1/2}. \quad (9)$$

This definition equips the probability measure space $\mathbf{Pr}_2(\Omega)$ with a proper metric. On this metric, the Wasserstein-2 gradient flow writes as:

$$\partial_t \rho = -\nabla_{W_2} F[\rho] = \nabla_{\theta} \cdot \left(\rho \nabla_{\theta} \frac{\delta F[\rho]}{\delta \rho} \right), \quad (10)$$

where $\frac{\delta F}{\delta \rho} : \Omega \rightarrow \mathbb{R}$ is the Fréchet derivative, and we usually term $\nabla_{\theta} \frac{\delta F}{\delta \rho}$ as the velocity field.

One nice structure of this W_2 gradient flow (10) is that it can be easily represented by discrete particles’ motion. Denoting the empirical measure on selected particles $\{\theta_i\}_{i=1}^N$,

$$\rho = \frac{1}{N} \sum_{i=1}^N \delta_{\theta_i}, \quad (11)$$

then McKean-Vlasov formulation states that particles θ_i moves according to the flow:

$$\dot{\theta}_i = -\nabla_{\theta} \frac{\delta F}{\delta \rho}(\theta_i), \quad \text{for } i = 1, \dots, N.$$

Complication may arise that (11) is a measure-valued solution, so (10) has to be interpreted in the weak sense. We refer interested readers to [5]. Although the numerical computation is done via finite particle simulation, we remark that the W_2 gradient flow (15) is the foundation to solving our continuous OED problem and encompasses both continuous and discrete types of probability distribution ρ .

3 Methodology for nonlinear design

In this section, we propose the nonlinear experimental design over the probability measure space $\mathbf{Pr}_2(\Omega)$. In particular, we examine the design problem (3), with the objective F defined following the OED criterion in the linear setting (7). We formulate this two-layer optimization problem in Section 3.1 by calling the Fisher information matrix \mathcal{I} . Gradient-flow structure is utilized to conduct the outer-layer optimization and we also provide the explicit formulas for computing the gradient. To execute this optimization, the Monte-Carlo particle method is deployed. In the outer-layer update, the particle velocity needs to be evaluated at the optimal inner layer solution. A brute-force computation calls for an inner-layer optimization solver for each update in the outer-layer, as described in Section 3.2. Unfortunately, this procedure is computationally challenging. In Section 3.3 we provide a simple modification to make the problem computationally much more feasible, owing to the implicit function theory.

3.1 Nonlinear design formulation

Firstly we lay out our formulation to conduct the nonlinear design, following similar criteria (7) for linear models discussed in Section 2.1.

To proceed, we define the Fisher information matrix:

$$\mathcal{I}[\rho; \boldsymbol{\sigma}] = \int_{\Omega} \mathcal{C}(\theta; \boldsymbol{\sigma}) \rho(\theta) d\theta \in \mathbb{R}^{d \times d} \quad \text{with} \quad \mathcal{C}(\cdot; \boldsymbol{\sigma}) = \nabla_{\boldsymbol{\sigma}} \mathcal{M}(\cdot; \boldsymbol{\sigma}) \nabla_{\boldsymbol{\sigma}} \mathcal{M}^{\top}(\cdot; \boldsymbol{\sigma}) \in \mathbb{R}^{d \times d}. \quad (12)$$

The Fisher information $\mathcal{I}[\rho; \boldsymbol{\sigma}]$ is a straightforward extension of the term $\mathbf{A}^{\top} \mathbf{A}[\rho]$ stated previously in Section 2.1, considering $\nabla_{\boldsymbol{\sigma}} \mathcal{M}(\theta; \boldsymbol{\sigma}) = \mathbf{A}(\theta, \cdot)$ in the linear case. Often it is also referred to as the Gauss-Newton Hessian. With the Fisher matrix, we formulate two criteria that resemble (7) and (8):

$$F^A[\rho; \boldsymbol{\sigma}] \equiv \text{Tr}(\mathcal{I}[\rho; \boldsymbol{\sigma}])^{-1}, \quad \text{and} \quad F^D[\rho; \boldsymbol{\sigma}] \equiv \log(\text{Det}(\mathcal{I}[\rho; \boldsymbol{\sigma}])). \quad (13)$$

When $\mathcal{I}[\rho; \boldsymbol{\sigma}]$ is evaluated at the inverse problem solution $\boldsymbol{\sigma} = \boldsymbol{\sigma}^*[\rho]$ (1), it represents the size of error in the solution when data is polluted. The nonlinear experimental design problems are now written as:

$$\text{A-optimal } \rho^A := \arg \min_{\rho \in \mathbf{Pr}_2(\Omega)} F^A[\rho; \boldsymbol{\sigma}^*[\rho]], \quad (14a)$$

$$\text{D-optimal } \rho^D := \arg \max_{\rho \in \mathbf{Pr}_2(\Omega)} F^D[\rho; \boldsymbol{\sigma}^*[\rho]], \quad (14b)$$

where the optimizer of the loss function is:

$$\boldsymbol{\sigma}^*[\rho] := \arg \min_{\boldsymbol{\sigma} \in \mathbb{R}^d} \text{Loss}[\boldsymbol{\sigma}; \rho] = \int_{\Omega} (\mathcal{M}(\theta; \boldsymbol{\sigma}) - \text{data}(\theta))^2 \rho(\theta) d\theta \quad (1).$$

Because the nonlinear OED criteria (14) only see the Fisher information at the global optimal point $\boldsymbol{\sigma}^*$ of the loss function, it describes the local sensitivity close to $\boldsymbol{\sigma}^*$.

3.2 Brute-force algorithm

We give a brute-force solver for the nonlinear OED (14). Noting that the outer-layer optimization is conducted over $\rho \in \mathbf{Pr}_2(\Omega)$, we propose to deploy the gradient flow equation outlined in (15). Namely, evaluated at the global optimizer $\boldsymbol{\sigma}^*[\rho]$, one can run the following PDE for updating ρ regarding the design criterion F (14):

$$\partial_t \rho = \nabla_{\theta} \cdot \left(\rho \nabla_{\theta} \frac{\delta F[\rho; \boldsymbol{\sigma}^*[\rho]]}{\delta \rho} \right). \quad (15)$$

We should stress that this evolution equation is highly nonlinear. Not only the velocity field $\nabla_{\theta} \frac{\delta F[\rho; \boldsymbol{\sigma}^*[\rho]]}{\delta \rho}$ itself depends on ρ , its second argument $\boldsymbol{\sigma}^*[\rho]$ also implicitly depends on ρ . Nevertheless, for every fixed $(\rho, \boldsymbol{\sigma})$, we can compute explicitly the velocity field, which is illustrated in the following:

$$\nabla_{\theta} \frac{\delta F^A[\rho; \boldsymbol{\sigma}]}{\delta \rho}(\theta) = -2 \left(\nabla_{\theta} \nabla_{\boldsymbol{\sigma}} \mathcal{M}^{\top}(\theta; \boldsymbol{\sigma}) \right) (\mathcal{I}[\rho; \boldsymbol{\sigma}])^{-2} \nabla_{\boldsymbol{\sigma}} \mathcal{M}(\theta; \boldsymbol{\sigma}) \in \mathbb{R}^{\dim(\Omega)}, \quad (16a)$$

$$\nabla_{\theta} \frac{\delta F^D[\rho; \boldsymbol{\sigma}]}{\delta \rho}(\theta) = 2 \left(\nabla_{\theta} \nabla_{\boldsymbol{\sigma}} \mathcal{M}^{\top}(\theta; \boldsymbol{\sigma}) \right) (\mathcal{I}[\rho; \boldsymbol{\sigma}])^{-1} \nabla_{\boldsymbol{\sigma}} \mathcal{M}(\theta; \boldsymbol{\sigma}) \in \mathbb{R}^{\dim(\Omega)}, \quad (16b)$$

where the notation $\mathcal{I}[\rho; \boldsymbol{\sigma}] \in \mathbb{R}^{d \times d}$ is the Fisher information matrix (12). The above calculation is similar to Proposition 3.1 in [37], except that this formulation is for nonlinear systems \mathcal{M} .

To numerically solve the gradient flow PDE (15), we employ the particle method. This means to rewrite ρ as an empirical measure of N particles $\{\theta_i\}_{i=1}^N$ and run the evolution of particles:

$$\rho = \frac{1}{N} \sum_{i=1}^N \delta_{\theta_i}, \quad \text{with} \quad \dot{\theta}_i = -\nabla_{\theta} \frac{\delta F[\rho; \boldsymbol{\sigma}^*[\rho]]}{\delta \rho}(\theta_i). \quad (17)$$

One can use the forward Euler to conduct the time discretization for (17). Let step size be Δt , then running (15) or (17) forward in time provides updates:

$$\theta_i^{t+1} = \theta_i^t + \Delta t \nabla_{\theta} \frac{\delta F[\rho^t; \boldsymbol{\sigma}^*[\rho^t]]}{\delta \rho}(\theta_i^t) \quad \text{for } i = 1, \dots, N, \quad (18)$$

with $\rho^t = \frac{1}{N} \sum_{i=1}^N \delta_{\theta_i^t}$ and $\boldsymbol{\sigma}^*[\rho^t]$ defined in (1) and obtained by running a sub-routine optimization.

Proposition 1. *Fix a set of particles $\{\theta_i\}_{i=1}^N$ and consider the empirical measure in (17). Let F^A and F^D defined in (13), we have:*

$$\nabla_{\theta} \frac{\delta F^A[\rho; \boldsymbol{\sigma}]}{\delta \rho}(\theta) = -2 \left(\nabla_{\theta} \nabla_{\boldsymbol{\sigma}} \mathcal{M}^{\top}(\theta; \boldsymbol{\sigma}) \right) \hat{\mathcal{I}}^{-2} \nabla_{\boldsymbol{\sigma}} \mathcal{M}(\theta; \boldsymbol{\sigma}) \in \mathbb{R}^{\dim(\Omega)}, \quad (19a)$$

$$\nabla_{\theta} \frac{\delta F^D[\rho; \boldsymbol{\sigma}]}{\delta \rho}(\theta) = 2 \left(\nabla_{\theta} \nabla_{\boldsymbol{\sigma}} \mathcal{M}^{\top}(\theta; \boldsymbol{\sigma}) \right) \hat{\mathcal{I}}^{-1} \nabla_{\boldsymbol{\sigma}} \mathcal{M}(\theta; \boldsymbol{\sigma}) \in \mathbb{R}^{\dim(\Omega)}, \quad (19b)$$

where the matrix $\hat{\mathcal{I}}$ is the discrete version of Fisher information (12):

$$\hat{\mathcal{I}} = \frac{1}{N} \sum_{i=1}^N \mathcal{C}(\theta_i; \boldsymbol{\sigma}) \in \mathbb{R}^{d \times d}.$$

The above proposition is an nonlinear extension to Proposition 3.4 of [37]. It is the result of (16) inserting the empirical measure (17).

The full standard algorithm is summarized below, where we mark the **outer-layer step for ρ in blue** and the **inner-layer step for $\boldsymbol{\sigma}^*$ in red**.

We remark in Algorithm 1, at iteration t , the outer-loop takes one gradient-descent step to move the particles to $\{\theta_i^{t+1}\}$, equivalently ρ^{t+1} . Next for the inner-loop optimization on solving $\boldsymbol{\sigma}^*[\rho^{t+1}] \equiv \boldsymbol{\sigma}^{*,t+1}$: line 4 - 8, we use the vanilla gradient-descent. The gradient computation uses its empirical representation $\rho = \frac{1}{N} \sum_{i=1}^N \delta_{\theta_i}$:

$$\nabla_{\boldsymbol{\sigma}} \text{Loss}[\boldsymbol{\sigma}; \rho] \equiv \nabla_{\boldsymbol{\sigma}} \text{Loss}(\boldsymbol{\sigma}; \{\theta_i\}) = \frac{2}{N} \sum_{i=1}^N \nabla_{\boldsymbol{\sigma}} \mathcal{M}(\theta_i; \boldsymbol{\sigma}) (\mathcal{M}(\theta_i; \boldsymbol{\sigma}) - \text{data}(\theta_i)). \quad (20)$$

Other optimization solvers can also be applied per user's choice.

Algorithm 1 Two-layer gradient flow algorithm

input: number of main and sub-routine iterations T, T' , time steps in main and sub-routine $\Delta t, \Delta t'$; initial particles $\theta_1^0, \dots, \theta_N^0 \subset \Omega$ and parameter $\sigma^{*,0} \in \mathbb{R}^d$ s.t.

$\sigma^{*,0} = \arg \min_{\sigma} \text{Loss}[\sigma; \rho^0]$.

output: empirical measure ρ (11) and inference parameter σ^* .

1: **for** $t = 0 : T - 1$ **do**

2: $\theta_i^{t+1} \leftarrow \theta_i^t + \Delta t \dot{\theta}_i \Big|_{\rho^t, \sigma^{*,t}}$ as done in (18)-(19) for all $i = 1, \dots, N$

3: $\rho^{t+1} \leftarrow \frac{1}{N} \sum_{i=1}^N \delta_{\theta_i^{t+1}}$ ▷ (I) update measure ρ

4: **initialize:** $\sigma^0 \leftarrow \sigma^{*,t}$

5: **for** $t' = 0 : T' - 1$ **do**

6: $\sigma^{t'+1} \leftarrow \sigma^{t'} - \Delta t' \nabla_{\sigma} \text{Loss}[\sigma^{t'}; \rho^{t+1}]$

7: **end for**

8: **return** $\sigma^{*,t+1} \leftarrow \sigma^{T'}$ ▷ (II) update parameter σ^*

9: **end for**

return $\rho \leftarrow \frac{1}{N} \sum_{i=1}^N \delta_{\theta_i^T}$ and $\sigma^* \leftarrow \sigma^{*,T}$.

3.3 Streamlined algorithm

The brute-force Algorithm 1 can be computationally intense. A big portion of the computation in Algorithm 1 is in line 4 - 8, i.e. obtaining the optimal $\sigma^{*,t}$ for each updated ρ^t . However, it is natural to suspect that if the outer-layer update from ρ^t to ρ^{t+1} is small, the associated optimum $\sigma^{*,t}$ should not change much, so starting the optimization fresh in this inner-layer optimization for every outer-iteration is wasteful.

Building on this intuition, in this subsection we provide a streamlined approach to re-use the computation from the previous iteration, and reduce the cost. This streamlined method is computationally efficient and avoids subroutines as seen in Algorithm 1. The key idea is to track the evolution of σ^* using the evolution of ρ or its particle representation $\{\theta_i\}_{i=1}^N$.

To see it, we first note that the optimum σ^* (1) always enjoys the first-order critical condition. Namely for each ρ , the optimum $\sigma^*[\rho]$ satisfies:

$$\nabla_{\sigma} \text{Loss}[\sigma^*[\rho]; \rho] = 2 \int_{\Omega} \nabla_{\sigma} \mathcal{M}(\theta; \sigma^*) (\mathcal{M}(\theta; \sigma^*) - \text{data}(\theta)) \rho(\theta) d\theta = \mathbf{0} \in \mathbb{R}^d.$$

This equation implicitly links $\sigma^*[\rho]$ with ρ . Due to implicit function theorem [42], if $f(x, y(x)) = 0$, then $\frac{\partial f}{\partial x} + \frac{\partial f}{\partial y} \frac{\partial y}{\partial x} = 0$. Given the evolution of $x(t)$, one has $\partial_x f \dot{x} + \partial_y f \dot{y} = 0$, providing the evolution of $\dot{y} = -(\partial_y f)^{-1} \partial_x f \dot{x}$. Applied to our context, by setting $x = \rho$, $y = \sigma^*[\rho]$ and $f = \nabla_{\sigma} \text{Loss}[\sigma^*[\rho]; \rho]$, we have the evolution of σ^* :

$$\frac{d\sigma^*}{dt} = -(\text{Hess}_{\sigma} \text{Loss}[\sigma^*; \rho])^{-1} \left(\int_{\Omega} \frac{\delta(\nabla_{\sigma} \text{Loss}[\sigma^*; \rho])}{\delta \rho}(\theta) \partial_t \rho(\theta) d\theta \right) \in \mathbb{R}^d. \quad (21)$$

Here $\text{Hess}_{\sigma} \text{Loss}[\sigma^*; \rho] \in \mathbb{R}^{d \times d}$ denotes the Hessian of the loss function (1) with input $\sigma = \sigma^*$, and the integral term of R.H.S. results in a vector in \mathbb{R}^d . We should note the slight difference compared to (12). As the outer-layer solution ρ changes, the inner-layer optimal solution $\sigma^*[\rho]$ changes accordingly, and (21) nicely characterizes how the evolution of ρ passes down to that of $\sigma^*[\rho]$.

Accordingly, in each iteration to update ρ , one can simply conduct the update of σ^* (21) forward in one time step, as opposed to triggering the optimization oracle all over showed in Algorithm 1.¹

Similar to Algorithm 1, one can simulate the gradient flow (15) using the particle method with (18). Viewing ρ as the empirical measure of N particles, then the updating formula (21) is rewritten into:

$$\dot{\sigma}^* = -(\text{Hess}_{\sigma} \text{Loss}(\sigma^*; \{\theta_j\}))^{-1} \left(\sum_{i=1}^N \frac{\partial(\nabla_{\sigma} \text{Loss}(\sigma^*; \{\theta_j\}))}{\partial \theta_i} \dot{\theta}_i \right) \quad (22)$$

Here we abbreviate the notation and denote $\text{Loss}(\sigma^*; \{\theta_j\}) = \text{Loss}[\sigma^*; \rho]$ for the empirical measure $\rho = \frac{1}{N} \sum_j \delta_{\theta_j}$. The particle-based evolution equation (22) takes the velocity of the particles $\dot{\theta}_j$ given by (19a) - (19b) depending on the design criterion. Furthermore, (22) calls for two complicated terms. Nevertheless they are straightforward computation and we list them below:

Proposition 2. *There are two terms in the formulation of velocity $\dot{\sigma}^*$ (22). Specifically,*

$$\begin{aligned} \text{Hess}_{\sigma} \text{Loss}(\sigma^*; \{\theta_j\}) &= \frac{2}{N} \sum_{j=1}^N \nabla_{\sigma} \mathcal{M}(\theta_j; \sigma^*) \nabla_{\sigma} \mathcal{M}^{\top}(\theta_j; \sigma^*) \\ &+ \frac{2}{N} \sum_{j=1}^N \text{Hess}_{\sigma} \mathcal{M}(\theta_j; \sigma^*) (\mathcal{M}(\theta_j; \sigma^*) - \text{data}(\theta_j)). \end{aligned} \quad (23)$$

$$\begin{aligned} \frac{\partial(\nabla_{\sigma} \text{Loss}(\sigma^*; \{\theta_j\}))}{\partial \theta_i} &= \frac{2}{N} \nabla_{\sigma} \mathcal{M}(\theta_i; \sigma^*) (\nabla_{\theta} \mathcal{M}(\theta_i; \sigma^*) - \nabla_{\theta} \text{data}(\theta_i)) \\ &+ \frac{2}{N} \nabla_{\theta} \nabla_{\sigma} \mathcal{M}(\theta_i; \sigma^*) (\mathcal{M}(\theta_i; \sigma^*) - \text{data}(\theta_i)). \end{aligned} \quad (24)$$

We summarize the aforementioned procedures in Algorithm 2.

Algorithm 2 Streamlined gradient flow algorithm

input: number of particles N ; number of iterations T ; time step Δt ;

initial particles $\theta_1^0, \dots, \theta_N^0 \subset \Omega$ and parameter $\sigma^{*,0}$ s.t. $\sigma^{*,0} = \arg \min \text{Loss}[\sigma, \rho^0]$.

output: empirical measure ρ (11) and parameter σ^* .

1: **for** $t = 0 : T - 1$ **do**

2: $\theta_i^{t+1} \leftarrow \theta_i^t + \Delta t \dot{\theta}_i \Big|_{\rho^t, \sigma^{*,t}}$ for all $i = 1, \dots, N$

3: $\rho^{t+1} \leftarrow \frac{1}{N} \sum_{i=1}^N \delta_{\theta_i^{t+1}}$ ▷ (I) update measure ρ

4: $\sigma^{*,t+1} \leftarrow \sigma^{*,t} + \Delta t \dot{\sigma}^* \Big|_{\rho^{t+1}, \sigma^{*,t}}$ ▷ (II) update parameter σ^*

5: **end for**

return $\rho \leftarrow \frac{1}{N} \sum_{i=1}^N \delta_{\theta_i^T}$, $\sigma^* \leftarrow \sigma^{*,T}$

This algorithm has improvement over Algorithm 1 in its computational complexity. Computationally, Algorithm 1 requires $\mathcal{O}(dNT')$ runtime per outer-loop, where the sample N comes from line 6: the gradient computation (20). In contrast, Algorithm 2 completely removes the inner-loop

¹Noting that the R.H.S. result in (21) is written in the form of matrix inversion and vector product $A^{-1}b$. Computationally, we can use the faster backslash operation $A \setminus b$.

with the T' dependence. The major computational cost comes from computing the velocity field. Following the velocity formula in (22), we have:

- Compute the Hessian (23): $\mathcal{O}(d^2N)$;
- Compute the partial derivatives (24): $\mathcal{O}(dN)$;
- Compute the updated $\dot{\theta}_i$ (17), (19): $\mathcal{O}(d^3 + d^2N)$;

meaning that the overall cost is $\mathcal{O}(d^3 + d^2N)$ per outer-loop.

4 Numerical experiment: Lorenz 63 system

We demonstrate the performance of our numerical solvers in this section using Lorenz 63 model [44] as an example. It is a simplified mathematical model for atmospheric convection and is nonlinear and aperiodic. Though deterministic, the solution nevertheless demonstrates chaotic phenomenon and thus is a widely studied model.

To examine the model: suppose we can take measurements along trajectory of the solution to infer parameters in the model, when should we probe into the model so that the collected data ensure the most stable recovery? We provide our numerical study in this section, by both using Algorithm 1 and Algorithm 2.

The model is three dimensional and writes as:

$$\begin{cases} \dot{x} = \alpha(y - x) \\ \dot{y} = x(\gamma - z) - y \\ \dot{z} = xy - \beta z, \end{cases} \quad (25)$$

with $\boldsymbol{\sigma} = (\alpha, \beta, \gamma) \in \mathbb{R}^3$ ($d = 3$) as the unknown coefficients to be inferred, and x, y, z as the state variables to be observed. As at atmospheric mode, x, y, z variables stand for respectively the convection rate, horizontal and vertical temperature variations, and α, γ, β are proportional to Prandtl number, Rayleigh number and dimension of the physical layer respectively. Throughout this section for computation, we set the ground-truth parameters are $\boldsymbol{\sigma}_{\text{true}} = (\alpha_{\text{true}}, \gamma_{\text{true}}, \beta_{\text{true}}) = (10, 28, 8/3)$. The initialization of the model is fixed as $x(0) = 1.5, y(0) = -1.5, z(0) = 25$. Simulation is conducted using forward Euler with stepsize $\Delta t = 10^{-4}$.

As an inverse problem, state variables are measured and the information is used to infer this 3-dimensional parameters $\boldsymbol{\sigma} = [\alpha, \gamma, \beta]^\top \in \mathbb{R}^3$ as in (1). Namely, the PtO map \mathcal{M} is defined as

$$\mathcal{M}(\theta; \boldsymbol{\sigma}), \quad \text{with } \theta = (c, t) \in \Omega = \{x, y, z\} \times [0, 3],$$

where c represents which one of the three coordinates to be observed. And t is the observing time and we set the observation window to be $[0, 3]$. This means one can measure $x(t)$ or $y(t)$ or $z(t)$ at some time t . The derivative terms with respect to the model parameters $\boldsymbol{\sigma} = [\alpha, \gamma, \beta]$ can be explicitly computed. According to the definition of the Jacobian:

$$J \doteq \nabla_{\boldsymbol{\sigma}} \mathcal{M} = \begin{bmatrix} \frac{\partial x}{\partial \alpha} & \frac{\partial x}{\partial \gamma} & \frac{\partial x}{\partial \beta} \\ \frac{\partial y}{\partial \alpha} & \frac{\partial y}{\partial \gamma} & \frac{\partial y}{\partial \beta} \\ \frac{\partial z}{\partial \alpha} & \frac{\partial z}{\partial \gamma} & \frac{\partial z}{\partial \beta} \end{bmatrix}, \quad (26)$$

and to compute them, we time-differentiate (25) to obtain:

$$\frac{d}{dt}J = \begin{bmatrix} -\alpha & \alpha & 0 \\ \gamma - z & -1 & -x \\ y & x & -\beta \end{bmatrix} \cdot J + \begin{bmatrix} y - x & 0 & 0 \\ 0 & x & 0 \\ 0 & 0 & -z \end{bmatrix}. \quad (27)$$

Since the initialization for the state variables are fixed, the initial data for these derivatives are 0, meaning $J(t = 0) = 0$. Solving this ODE system gives us the evaluation of J for all time. In Fig. 1 we plot the trajectory of Lorenz 63 model the gradients of three state variables at the ground-truth σ_{true} .

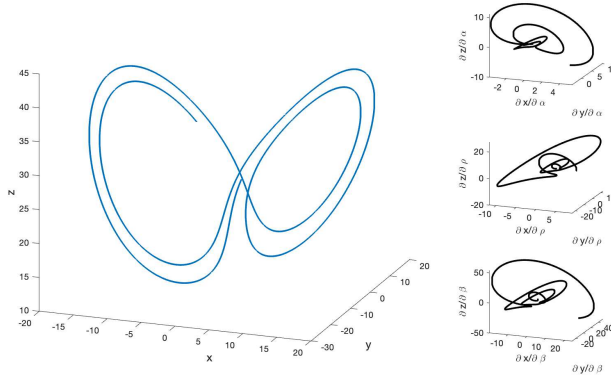


Figure 1: Lorenz 63 model (25) (left) and its gradient terms (27) (right).

One important feature of Lorenz 63 system is that its solution sensitively depends on the parameter configuration. A small perturbation to the parameter induces large deviation of the solution. As seen in Fig. 2, when σ is chosen as a random variable according to $\sigma_{\text{true}} + 0.1\mathcal{N}(0, \mathbf{I}_3)$, the discrepancy between the two solutions is large.

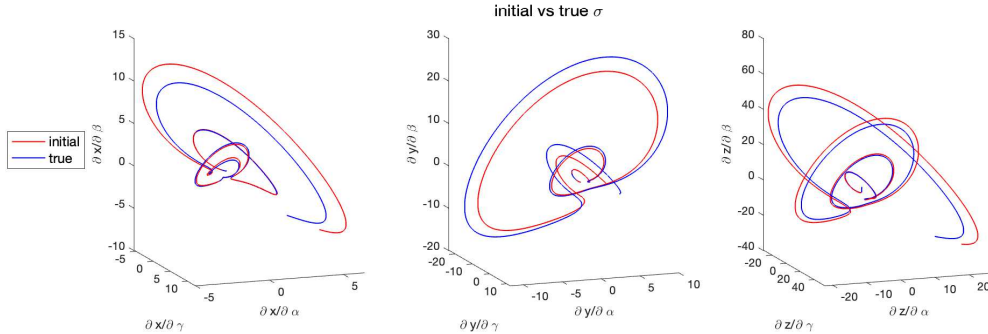


Figure 2: The comparison of $\nabla_{\sigma}\mathcal{M}(:,\sigma)$ and $\nabla_{\sigma}\mathcal{M}(:,\sigma_{\text{true}})$, with σ chosen from $\sigma_{\text{true}} + 0.1\mathcal{N}(0, \mathbf{I}_3)$.

Now we proceed with the experimental design, that is to select the best time points to observe from one of the three state variables for the optimal reconstruction of parameters. Since there are three possible choices of state variables to measure, we denote the design measure ρ as a combination of marginal distributions ρ_x, ρ_y, ρ_z , all supported on $[0, 3]$.

Below in Section 4.1 and Section 4.2 respectively we report the numerical performances of our algorithm for D-optimal (14b) and A-optimal (14a) design criteria. Each experiment is ran 20 times with each simulation having different particle sampling realizations from the same initial design measure ρ . To examine the performance of the algorithm, the evaluation methods include calculating the following four quantities:

1. Design objective value: F^A (14a) or F^D (14b)
2. Parameter solution error $\|\boldsymbol{\sigma}^* - \boldsymbol{\sigma}_{\text{true}}\|_2$
3. Optimization Loss $[\boldsymbol{\sigma}^*; \rho]$ (1)
4. Gradient norm $\|\nabla_{\boldsymbol{\sigma}} \text{Loss}\|_2$.

We will plot their evolutions along the algorithm’s iterations.

4.1 D-optimal design

We report numerical results for D-optimal design (14b) on the Lorenz 63 model. To initialize the algorithm, we set $N = 60$, with 20 for each state variable, meaning $\rho_x \approx \frac{1}{20} \sum_i \delta_{t,x,i}$, and similar approximation is applied to ρ_y, ρ_z as well. The initialization ρ^0 set to be uniform distribution on the time window $[0, 3]$. The initial $\boldsymbol{\sigma}^0$ is drawn from $\boldsymbol{\sigma}_{\text{true}} + 0.1\mathcal{N}(0, \mathbf{I}_3)$. We implement the brute-force gradient flow Algorithm 1 for D-optimal design. The outer-layer hyperparameters are $T = 50, \Delta t = 10^{-5}$ and the inner-layer’s are $T' = 20, \Delta t' = 10^{-3}$.

In Fig. 3, we plot the marginal distributions of $\rho : \rho_x, \rho_y, \rho_z$ before and after running the algorithm. At the initial stage, ρ^0 , seen on top row, is sampled uniformly over Ω , and as iterations propagate, the algorithm’s output of the design measure ρ eventually concentrate in specific time slots (bottom row). The spikes in the density indicate those are the times where measurements are important. We should note that the three variables are important to observe at slightly different times because the marginal distributions over the three coordinates show different patterns.

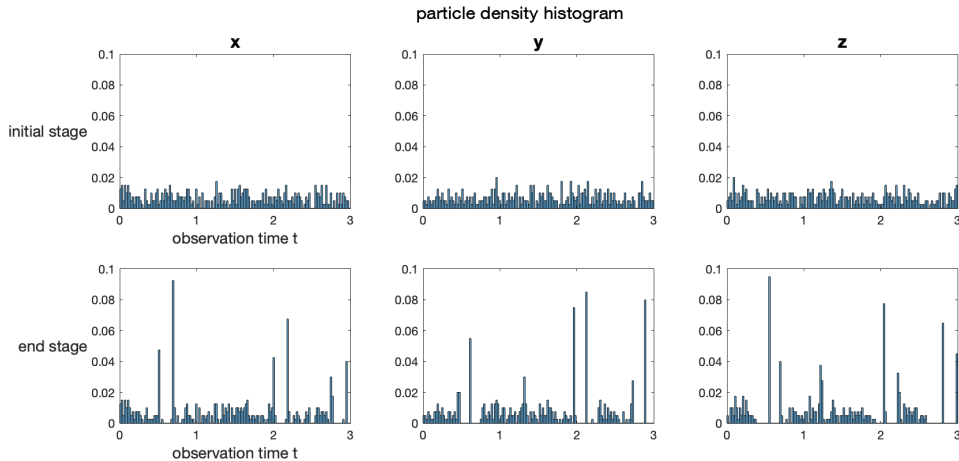


Figure 3: D-optimal design measures for x, y, z observables represented as particle density histograms. The top row is the three marginal distributions of the initial guess ρ^0 (that we set to be uniform over $[0, 3]$). The bottom row is the marginal distributions of the output of Algorithm 1.

In this example, since we know the ground-truth σ_{true} , we can compute the reference solution for benchmarking. To do so, we fix $\sigma = \sigma_{\text{true}}$ and solve the OED problem (14b) $\rho^{D,\text{true}} := \arg \min F^D[\rho; \sigma_{\text{true}}]$ with an extremely large N and T ($N = 10000$, and $T = 1000$). In this case, the ground-truth σ_{true} is already achieved, and thus the inner-loop of the two-layer optimization is completely omitted. In Fig. 4 we show the density histogram (marginal) of the found design measure ρ . Spikes exhibit the principal observation time. We are able to see that the benchmark spikes are aligned with our adaptive design results by comparing Fig. 3 and Fig. 4.

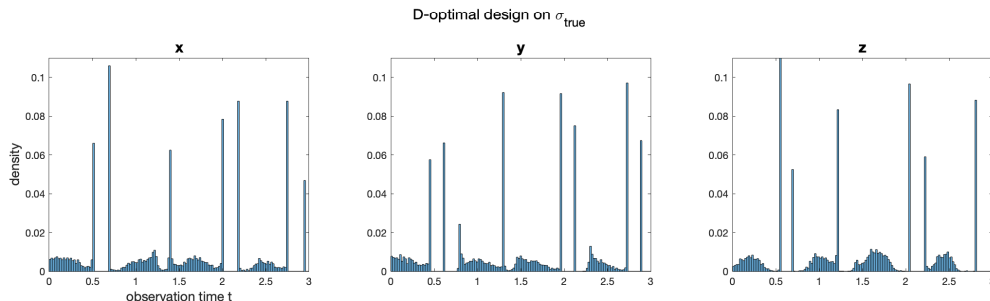
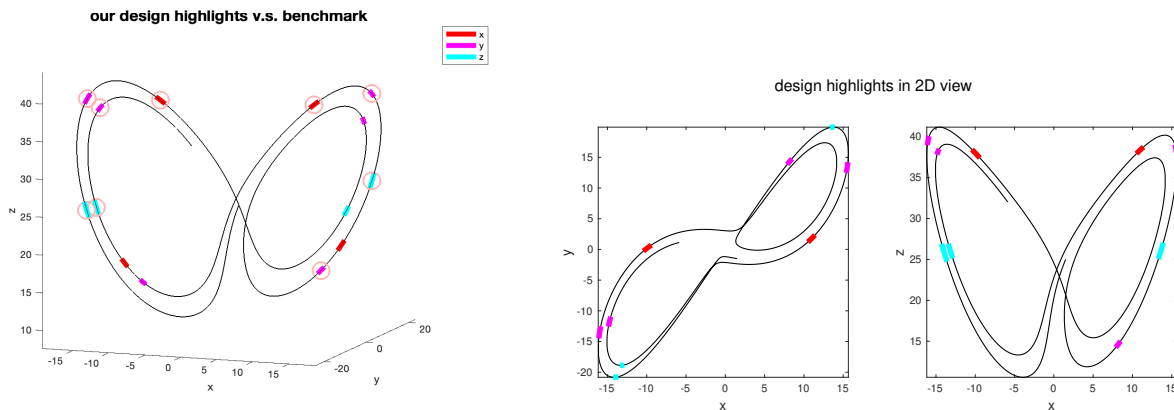


Figure 4: D-optimal benchmark design measures run on the ground-truth parameters σ_{true} .

We now examine these observation time of high importance more closely. Setting the density threshold as 5%, we identify the time bins whose density values are above this cut-off from the previously obtained histograms in Fig. 3- Fig. 4, and then highlight these selected time slots in Fig. 5 on the dynamical systems. Compared with the benchmark solution, seen in (a), we notice that the highlighting points selected by our algorithm recover most of those from the reference solution (9 out of 14). The circled ones have been identified by our algorithm, which are a subset of all benchmark highlights marked on the Lorenz model. The red, pink and blue represent the important time bins recognized by x , y , and z observables respectively. Also note that the three state variables are selected at different times. Further in Fig. 5 (b), it is interesting that some highlighted time points are extremal points of certain coordinate in the Lorenz 63 model \mathcal{M} .



(a) D-optimal design measure highlights in comparison with the benchmark important points.

(b) Importance points are extreme points on the model

Figure 5: D-optimal design highlights.

We now quantitatively validate the algorithm. In Fig. 6, we plot the time evolution of the four metrics. The four panels display the evolution of the D-optimal design score (14b), the reconstruction error in σ , the loss function (1), and the gradient norm $\|\nabla_{\sigma}\mathcal{M}\|_2$. As expected, the D-optimal design score increases to platform, and all other quantities decay to zero along iterations. The shaded area indicates the standard deviation of 20 independent runs.

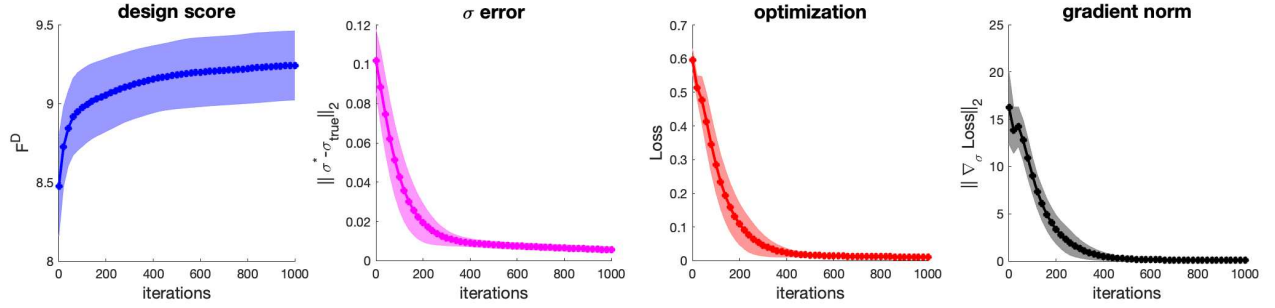


Figure 6: The four different metrics when initial sampling ρ^0 is uniform.

After the design procedure, we are to select experiments and provide the best reconstruction of the unknown parameter σ . To see that, we examine the performance of optimization for reconstructing σ (1) using strategic sampling (the output of our algorithm) and ρ^0 (uniform sampling). More specifically,

- Strategic sampling: the design measure as the output of Algorithm 1 shown in Fig. 3. We only sample from the important time slots marked in Fig. 5, and in each slot we sample 7 time points randomly. Since we have identified 9 time bins, the total sampled particles in one simulation is 63.
- Uniform sampling: This is to uniformly sample 21 points from each state variable x, y, z on the time window $[0, 3]$, so that the total number of sampled particles is also 63.

The reconstruction comparison is shown in Fig. 7. It is clear that utilizing observations drawn from the optimal design measure produces faster convergence rate on both approximating the unknown model parameters in panel (a) and minimizing the optimization loss in (b). Particularly in (b), the loss measured by strategically sampled observations is initially higher than the loss produced by uniform sampling. However the loss in blue curve drops significantly faster and outperforms the uniform sampling method (red) immediately.

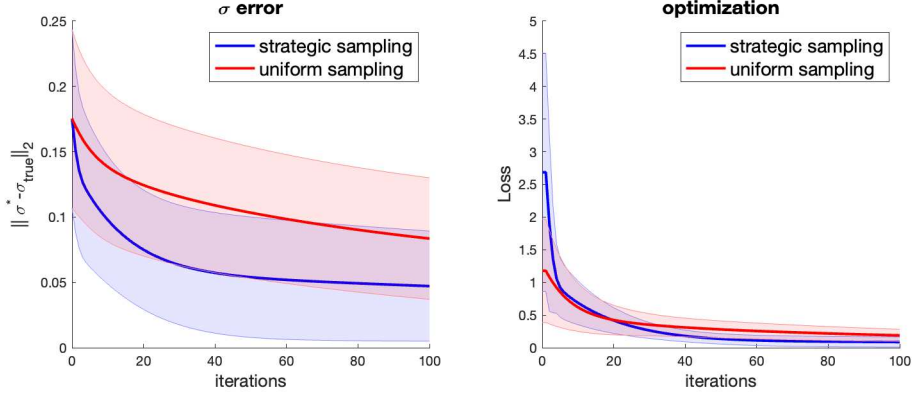


Figure 7: Convergence comparisons: experiments that we choose provide faster error decay in the σ reconstruction than those that are uniformly distributed over time.

Finally, we test the proposed nonlinear design Algorithm 2 with a more crafted initialization, a.k.a. a warm start on the measure ρ . The initial choice ρ^0 is inspired by the benchmark design measure shown in Fig. 4. In particular, for each variable x, y, z , we select the top 6 time bins that have the highest histogram values, and uniformly draw 3 samples per bin. So we have 18 samples per observable and 54 samples in total. This warm start of initial data is the input of Algorithm 2 and we run the algorithm for $T = 300$ with $\Delta t = 10^{-6}$. The results are presented in Fig. 9. For comparison, we plot the histogram for each ρ_x, ρ_y, ρ_z before and after the algorithm run in selected time bins. We noticed that concentration continues along the algorithm iterations. Even we start with samples drawn from 6 very narrow time windows, the output design measure has even sharper concentration and shrinks the observation time domain further. The four different error metrics are plotted in Fig. 8. As expected, the D-optimal design value rises till convergence, and σ reconstruction error, loss function and $\|\nabla_{\sigma} \text{Loss}\|_2$ decrease.

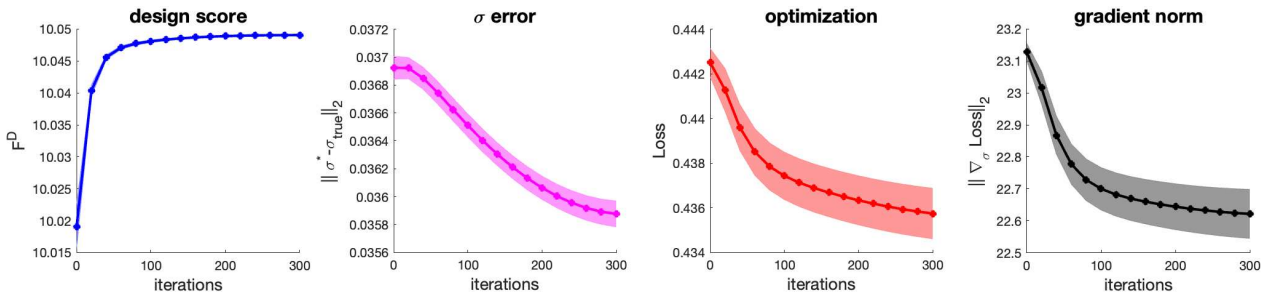


Figure 8: The four different metrics when initial sampling ρ^0 is set as a warm start.

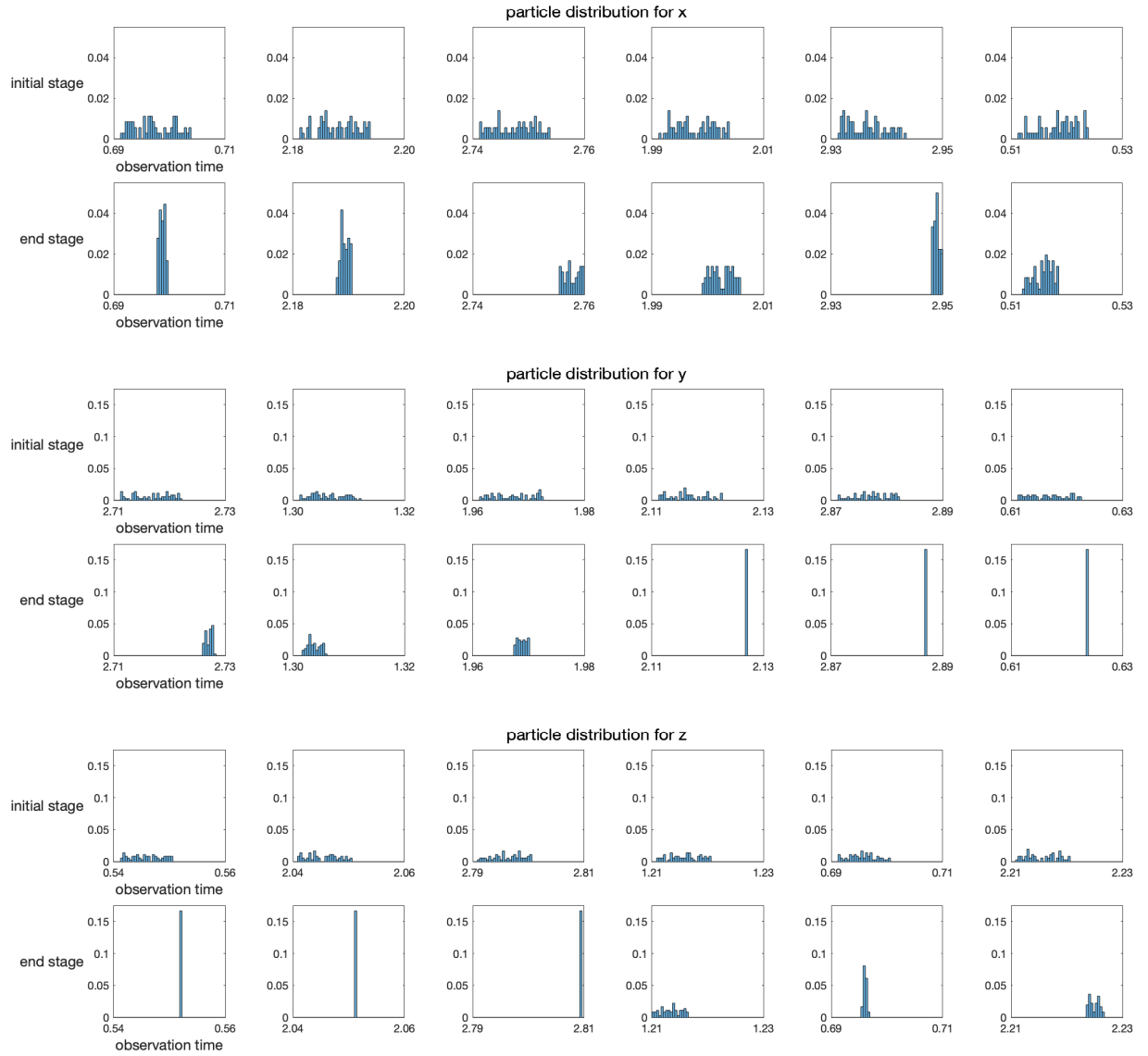


Figure 9: D-optimal warm-start case: we present the marginal distributions ρ_x, ρ_y, ρ_z at the beginning and final stages of Algorithm 2, zooming in 6 important time bins.

4.2 A-optimal design

We now report the performance of proposed algorithms with A-optimal criterion (14a). The testing methodology follows that of D-optimal design.

When initial distribution is uniform, we run Algorithm 1 with T and Δt set to be 1000 and 10^{-5} respectively. In Fig. 10 We find the samples get concentrated over a few time windows. In Fig. 11 we plot the benchmark A-optimal solution by setting $\sigma = \sigma_{\text{true}}$. The observation highlights are marked in Fig. 12. Once again we use 5% as the cut-off threshold. The benchmark solution identifies 10 time windows to conduct experiment, and our algorithm recovers 7 of them. It is also interesting to discover that the density spikes are located in relatively the same slots for all x, y, z variables. This may indicate the strong correlation of the three observables in the A-optimal design case. The evaluation metrics are plotted in Fig. 13. As expected, A-optimal design score, σ reconstruction error, loss function (1), and $\|\nabla_{\sigma} \text{Loss}\|_2$ all decay in iterations along the algorithm.

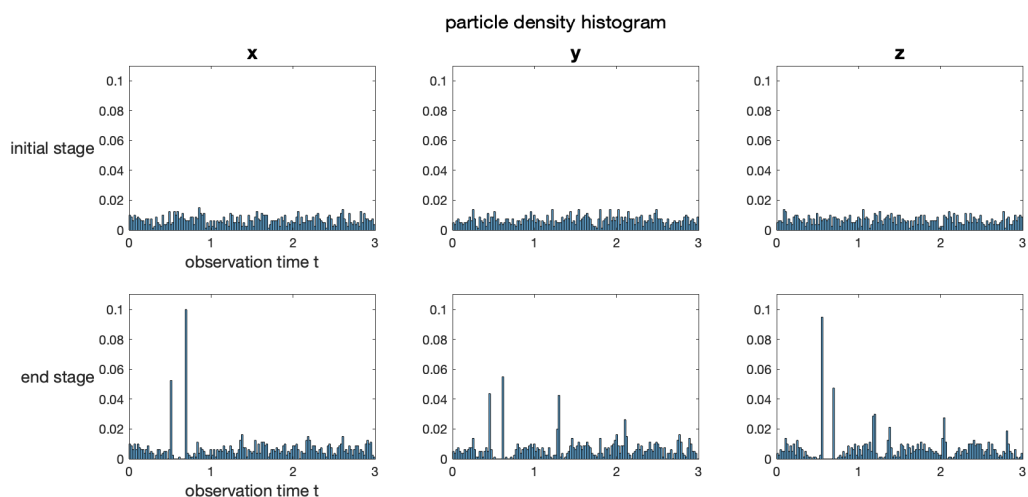


Figure 10: A-optimal design measures on each observable x, y, z . The top row is the initial uniform distribution. The bottom row is the Algorithm 1-optimized distribution.

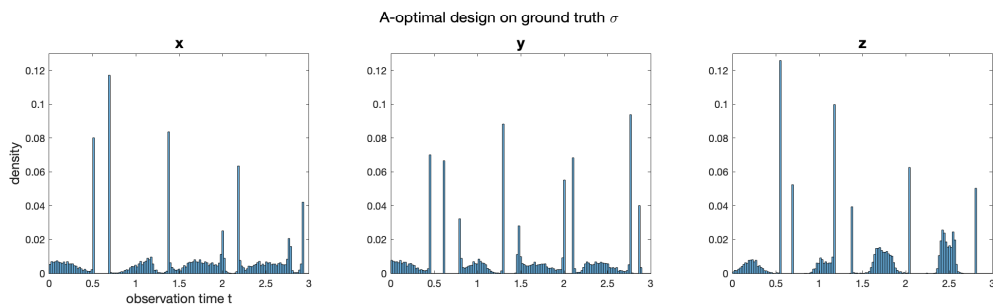


Figure 11: A-optimal benchmark design measures run on the ground-truth σ_{true}

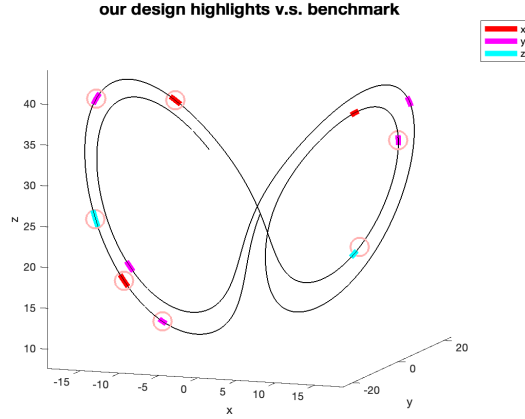


Figure 12: A-optimal design highlights by Algorithm 1 (in red circles) recover 7 out of the total 9 benchmark important spots. The three marking colors distinguish the results for x, y, z observables respectively.

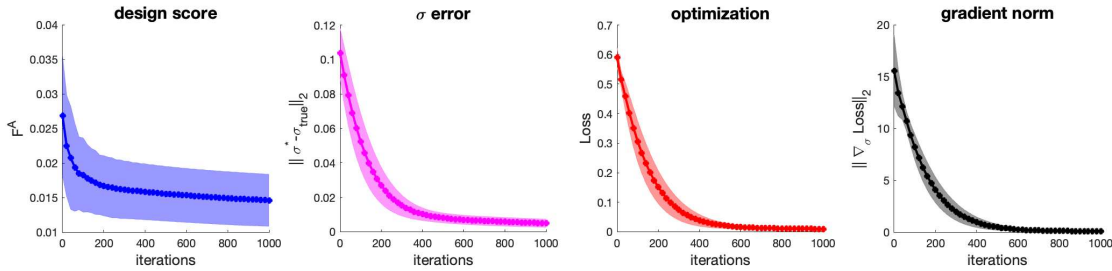


Figure 13: The four testing metrics when the initial ρ^0 is uniform distribution.

We also implement the Algorithm 2 using A-optimal design with a warm start for ρ^0 setting $T = 3000, \Delta t = 10^{-1}$. At the initial time, the particles are sampled from only important time windows. In particular, we choose the top 6 density spikes for each observable x, y, z from the benchmark result showed in Fig. 11. The optimal design measure $[\rho_x, \rho_y, \rho_z]$ as the output of Algorithm 2 are presented in Fig. 15. Comparing the initial and final distributions, most particles remain roughly within the same time windows, and in some bins, the particles proceed for sharper concentrations. The A-optimal objective (14a) is shown in Fig. 14. The value for F^A only drops slightly, implying that the initial ρ^0 is already close to the optimum ρ^A , making the effect of OED update minor.

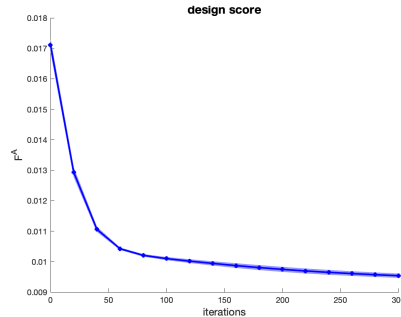


Figure 14: A-optimal design objective (14a) decreases along Algorithm 2 iterations when the initialization ρ^0 is set as a warm start.

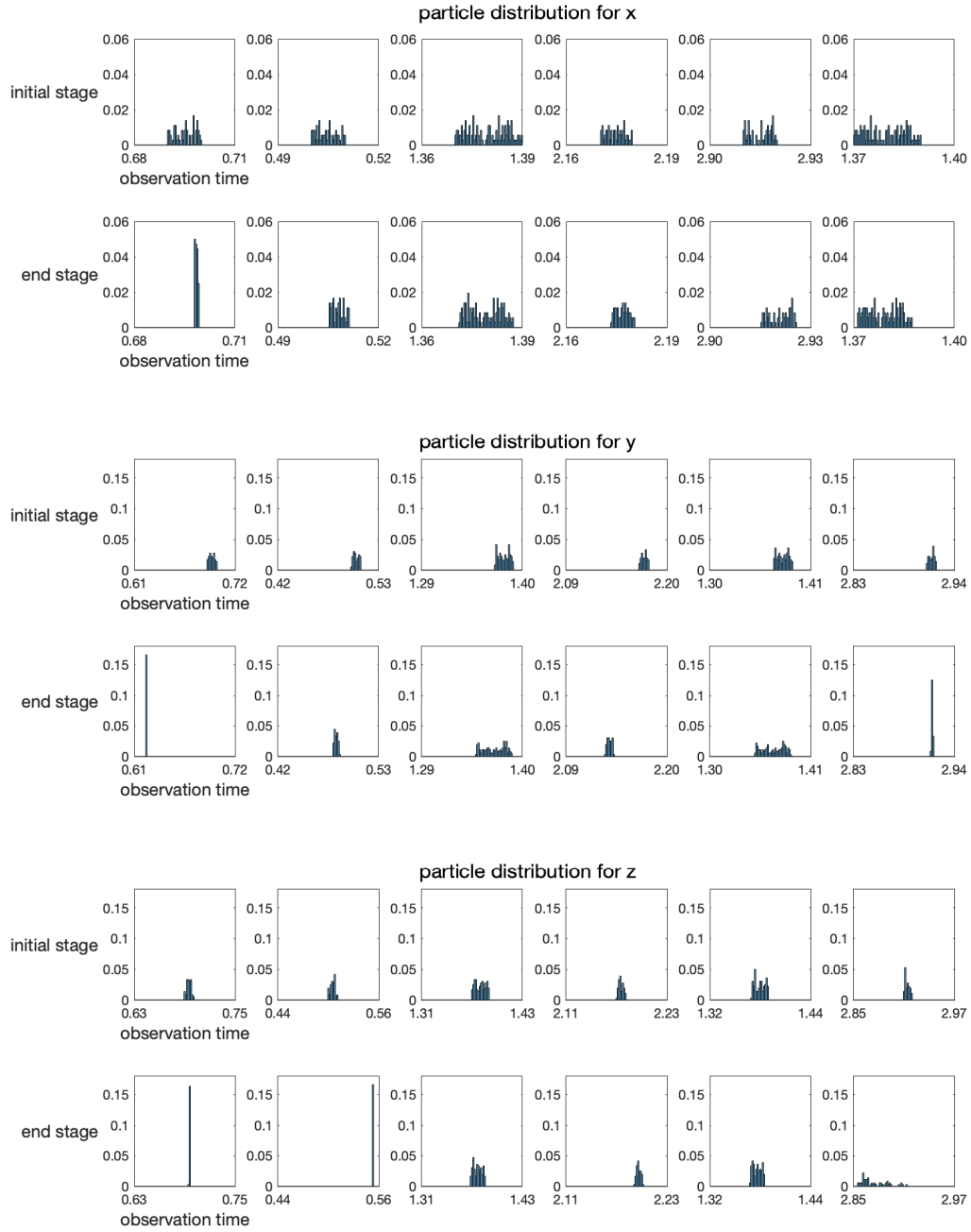


Figure 15: A-optimal design warm-start case: we present the marginal distribution ρ_x, ρ_y, ρ_z at the initial and final stages of Algorithm 2, zooming in 6 important time bins for each observable x, y, z .

5 Numerical experiment: Schrödinger equation

After a thorough study for Lorenz system, we now switch gear to a simplified Schrödinger equation model [25] using Algorithm 2 for picking important measurements. Unlike Lorenz system that is dynamical in time, Schrödinger equation describes a steady state solution, and thus measurements are taken in space. We are tasked to find the measurement locations in space that contain the best information to recover the unknown potential.

The simplified version of the Schrödinger model writes as

$$\begin{cases} u'' + \sigma u = S(x), & x \in [0, 1] \\ u|_{x=0,1} = 0. \end{cases} \quad (28)$$

where we set the domain $x \in [0, 1]$ and deployed zero boundary condition. Different sources $S(x)$ are injected into the model and measurements $u(x)$ are taken to infer the unknown potential function $\sigma \in L^2([0, 1])$. In our numerical test, we set the ground-truth potential function σ_{true} as a Gaussian mixture, see details in Section 5.1-Section 5.2 below.

For the purpose of designing experiments, we should note that we can design the form of $S(x)$ and the detector location. Meaning we can inject source S at $\theta^1 \in [0, 1]$ by setting $S(x) = \delta_{\theta^1}$, and measure the solution u_{θ^1} at location $\theta^2 \in [0, 1]$. Therefore, mathematically the design space is $\theta = (\theta^1, \theta^2) \in \Omega = [0, 1]^2$ and the observation has the form of:

$$\mathcal{M}(\theta; \sigma) = u_{\theta^1}(\theta^2) \in \mathbb{R}.$$

Running the classical calculus-of-variable argument, one can compute the Fréchet derivative of \mathcal{M} with respect to σ and obtain:

$$\frac{\delta \mathcal{M}(\theta; \sigma)}{\delta \sigma} = u_{\theta^1} v_{\theta^2},$$

where u_{θ^1} and v_{θ^2} solve the forward and adjoint model respectively:

$$\text{forward : } \begin{cases} u''_{\theta^1} + \sigma u_{\theta^1} = \delta_{\theta^1}, & x \in [0, 1] \\ u_{\theta^1} = 0, & x = 0, 1, \end{cases} \quad \text{adjoint : } \begin{cases} v''_{\theta^2} + \sigma v_{\theta^2} = \delta_{\theta^2}, & x \in [0, 1] \\ v_{\theta^2} = 0, & x = 0, 1. \end{cases}$$

Numerically, we represent the function $\sigma(x)$ as a d -dimensional vector $\boldsymbol{\sigma}$ via a basis function set $\{\psi_k\}_{k=1}^d$, namely $\sigma(x) \approx \sum_{k=1}^d \sigma_k \psi_k(x)$, with $\boldsymbol{\sigma} = [\sigma_1, \dots, \sigma_d]^\top$. In this discrete space, the above Fréchet derivative transfers to a gradient vector with respect to $\boldsymbol{\sigma} \in \mathbb{R}^d$:

$$\partial_{\sigma_k} \mathcal{M}(\theta; \boldsymbol{\sigma}) = (\nabla_{\boldsymbol{\sigma}} \mathcal{M}(\theta; \boldsymbol{\sigma}))_k = \left\langle \frac{\delta \mathcal{M}(\theta; \boldsymbol{\sigma})}{\delta \sigma}, \psi_k \right\rangle = \langle u_{\theta^1} v_{\theta^2}, \psi_k \rangle.$$

We use the finite difference method to solve for the forward and adjoint models. Accordingly, it is natural to decompose the domain $[0, 1]$ into d equi-spaced cells, and set the basis $\{\psi_k\}_{k=1}^d$ to be characteristic functions over k -th cell. Numerically we use $d = 100$.

The particle gradient flow Algorithm 2 alternatively updates for $\{\theta_i\}_{i=1}^N$ and $\boldsymbol{\sigma} \in \mathbb{R}^{100}$. For each test, we will specify the ground-truth $\boldsymbol{\sigma}_{\text{true}}$, and the observation is then set to be $\text{data}(\theta) = \mathcal{M}(\theta; \boldsymbol{\sigma}_{\text{true}}) + \epsilon$ with the additive noise follows independent Gaussian distribution $\epsilon \sim 0.1 \mathcal{N}(0, 1)$.

To run Algorithm 2, we need to specify initial distribution ρ^0 and initial guess for $\boldsymbol{\sigma}$. In both A-optimal and D-optimal designs, we use both uniform distribution and a warm-start distribution

for ρ^0 , and our initial guess for σ is set to be $\sigma_{\text{true}} + 2U[0, 1]^{100}$ where U denotes the uniform distribution. To represent ρ^0 , we can draw N samples $\{\theta_i\}_{i=1}^N$. Since each sampling will lead to slightly different behavior, we run the simulation 10 times and plot their average behavior below. To reduce the computation burden, we give the approximated calculation for the velocity term $\dot{\sigma}^*$ (22). As the distance between σ^* and the ground-truth σ_{true} is close, this discrepancy $\mathcal{M}(\theta; \sigma^*) - \text{data}(\theta)$ can be omitted. Hence we can drop the second lines of both formulas (23) and (24), which avoids probing in the nontrivial terms $\text{Hess}_{\sigma}\mathcal{M}$ and $\nabla_{\theta}\nabla_{\sigma}\mathcal{M}$.

5.1 A-optimal design

The ground-truth media σ_{true} is set to be a Gaussian mixture:

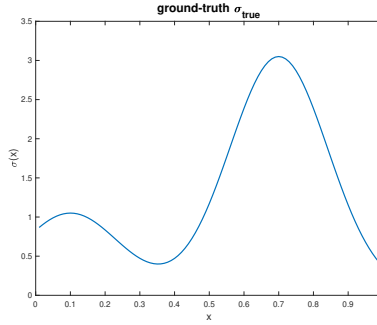


Figure 16: Ground-truth $\sigma_{\text{true}} = \exp\left(-\frac{x-0.1}{0.2}\right)^2 + 3 \exp\left(-\frac{x-0.7}{0.2}\right)^2 + 0.05$.

In the first test, we set the initial distribution $\rho^0 = U([0, 1]^2)$, and this ρ^0 is represented by $N = 10,000$ samples. To kick off the simulation, we first need to compute the first-order criticality point $\sigma^*[\rho^0]$. To do so we run the inner optimization with $T = 2000$ iterations with step size set to be $\Delta t = 10^{-7}$. We show three snapshots of ρ^t in Fig. 17. Along the evolution, the design measure ρ picks up the diagonal information, indicating that the measurements are the most informative when the source θ^1 and detector θ^2 are in close proximity. In Fig. 18, we plot three metrics: A-optimal score F^A (14a) (in log-scale), L^2 reconstruction error $\|\sigma^* - \sigma_{\text{true}}\|_2$, and the loss function (1). They all drop along iterations, suggesting the adaptive gradient flow Algorithm 2 works successfully for A-optimal design. In the last panel of Fig. 18, we also demonstrate the reconstructed σ^* at the beginning and end of the algorithm run, as compared to the ground-truth. Note that the initial distribution $\sigma^{*,0}$ (red) is very jagged while the final solution $\sigma^{*,T}$ (yellow) closely fits the true σ_{true} (blue).

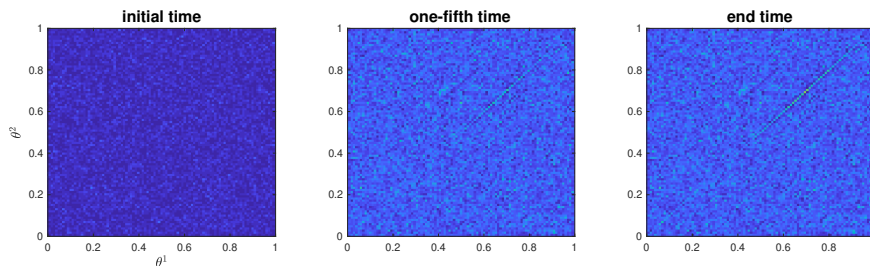


Figure 17: A-optimal design measure at three different snapshots, when ρ^0 is the uniform distribution on $\Omega = [0, 1]^2$.

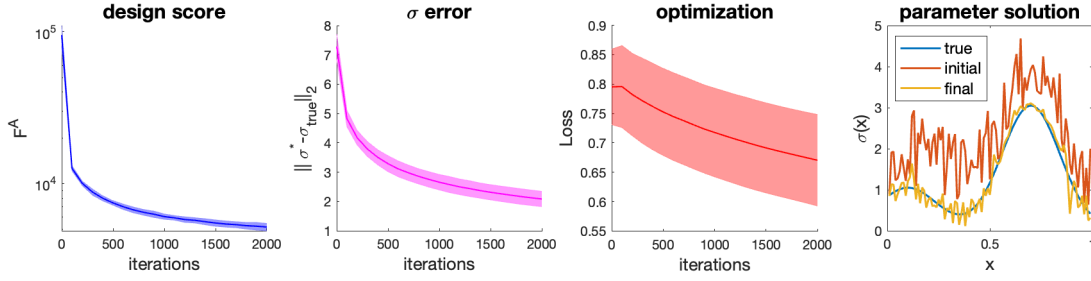
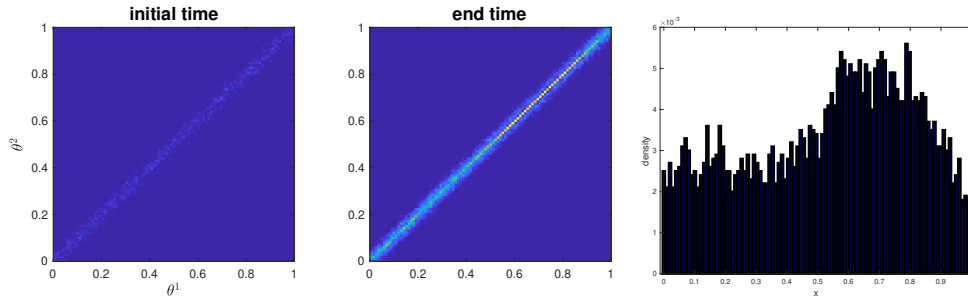


Figure 18: The initialization ρ^0 is the uniform distribution on $[0, 1]^2$. The three metrics from the left exhibits the decay of A-optimal objective (14a) and other errors. The rightmost panel shows the reconstructed σ^* at initial (red) and final (yellow) stage of the algorithm, in comparison to the ground-truth (blue).

In the second test, we use the warm-start initialization and set our beginning distribution ρ^0 to be close to the optimal ρ indicated from above test. Indeed, as observed from output in Fig. 17, the design measure ρ concentrates along the diagonal line, showing the data pairs with $\theta^1 = \theta^2$ should contain most information. So we set $\theta = (\theta^1, \theta^2)$ to be drawn according to $\theta^1 - \theta^2 \sim 0.002\mathcal{N}(0, 1)$, meaning the initial ρ^0 takes on the diagonal stripe in the design space $\Omega = [0, 1]^2$. The number of sampled particles is set to be $N = 1000$. We run A-optimal design using Algorithm 2 and set the step size to be $\Delta t = 10^{-6}$ with $T = 1000$. We show the results in Fig. 19. In panel (a), we compare the initial distribution with the final output of Algorithm 2. It is clear that the algorithm pushes the particles even more concentrated along the diagonal. In panel (b), we show the histogram of particles constrained on the diagonal line: The distribution roughly represents the ground-truth σ_{true} shape (Fig. 16). It suggests that most informative design variables (θ^1, θ^2) are obtained by setting the source and detector at locations where σ_{true} achieves higher values. Similar to the test before, we evaluate the metrics and plot them as a function of iterations. In Fig. 20, we see that the A-design score, L^2 error of the reconstruction of σ and the loss function all decay. While the initial guess for σ (red) is very off from the ground-truth (blue), the output of the algorithm (yellow) recovers σ_{true} .



(a) A-optimal design measure at the start and final stages of Algorithm 2, with the initialization ρ^0 concentrating around the diagonal stripe.

(b) Particle histogram on the diagonal line at the final stage.

Figure 19: A-optimal warm-start case.

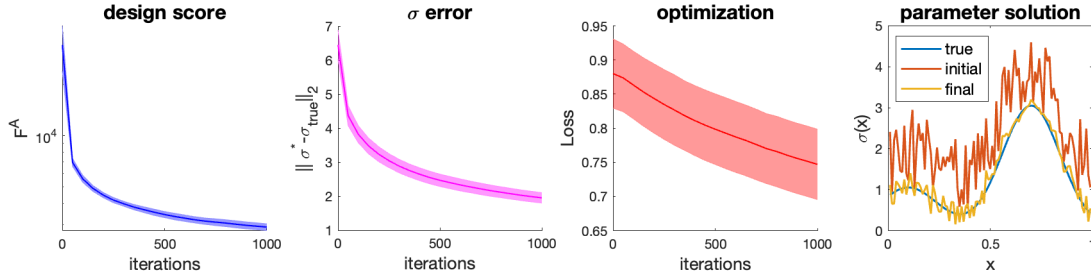


Figure 20: A-optimal warm-start case: the initial ρ^0 concentrates along the diagonal. The three metrics exhibits the decay of design objective and other errors. The rightmost panel shows the reconstructed σ^* at initial and final stage of the algorithm, in comparison to the ground-truth.

5.2 D-optimal design

We now report results obtained by Algorithm 2 on the D-optimal design criterion (14b). In Fig. 21 we plot the ground-truth potential function σ_{true} . Two tests will be presented, in which we use the initialization ρ^0 as the uniform distribution on $\Omega = [0, 1]^2$ and a warm-start that concentrates along the diagonal line respectively. In both tests, the initial guess for σ^0 is $\sigma_{\text{true}} + U[0, 1]^{100}$.

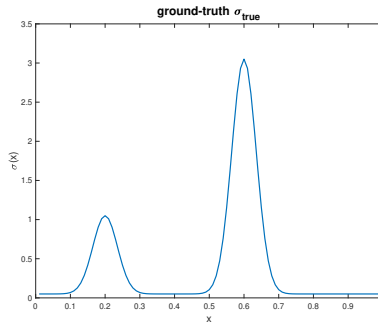


Figure 21: Ground-truth media $\sigma_{\text{true}} = \exp\left(-\frac{x-0.2}{0.05}\right)^2 + 3 \exp\left(-\frac{x-0.6}{0.05}\right)^2 + 0.05$.

We start the experiment with uniform initialization $\rho^0 = U([0, 1]^2)$. In this test, we start with $N = 10,000$ samples uniformly drawn from ρ^0 , and run Algorithm 2 with $\Delta t = 10^{-2}$ and $T = 500$.

In Fig. 22, we show the evolution of ρ . A similar pattern is observed compared to the A-optimal design above. As iterations extend, the particles gradually accumulate along the diagonal line. In Fig. 23, we observe the D-optimal score (14b) increases along iterations, and the L^2 norm of the reconstruction for σ and the loss function both decay. Moreover in the right plot of Fig. 23, even though the initial guess of σ (red) is far from the ground-truth σ_{true} (blue), our final output (yellow) of Algorithm 2 captures the true potential very well.

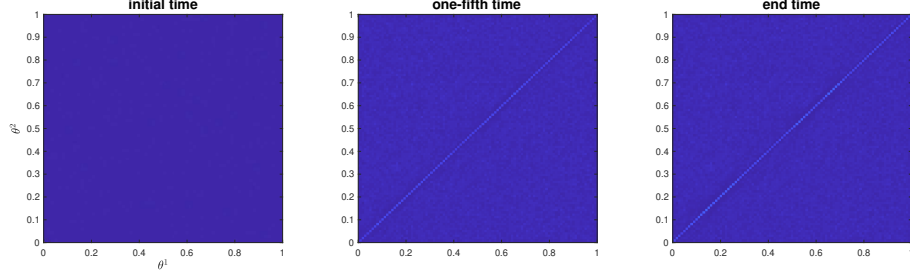


Figure 22: D-optimal design measure at three different snapshots when ρ^0 is the uniform distribution on $[0, 1]^2$.

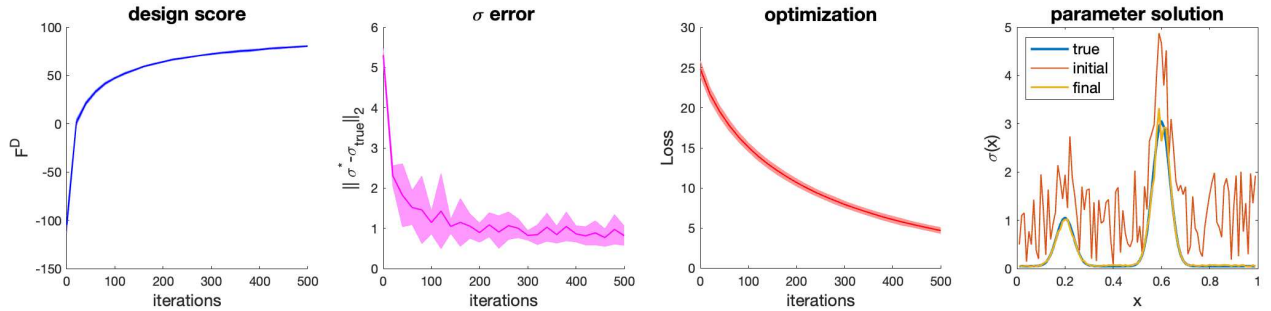


Figure 23: The initialization ρ^0 is the uniform distribution on $[0, 1]^2$. D-design score (14b) rises to platform, while the reconstruction error and the loss function both decay along iterations. The rightmost panel shows the reconstructed σ^* at initial and final stage of Algorithm 2, in comparison to the ground-truth.

In the second test, we craft our initial measure ρ^0 to be a warm start, where samples are centered along the diagonal line of $\Omega = [0, 1]^2$. We sample $N = 1000$ particles along the diagonal stripe, with the same strategy as described in Section 5.1, and run Algorithm 2 with step size $\Delta t = 10^{-2}$ with total iteration numbers $T = 500$. We plot the design measure in panel (a) of Fig. 24, and the histogram of samples constrained on the diagonal line in panel (b). In the D-optimal regime, while it is still true that experiments with same source and detector locations are preferred, i.e. $\theta^1 \approx \theta^2$, the D-optimal objective does not seem to favor any locations on the diagonal line. In Fig. 25, we also plot the increase of the D-design score (14b), and the decay of the reconstruction error and loss function along iterations. Similar to other cases, though the initial guess for σ is very from from the ground-truth, the output of Algorithm 2 successfully reconstruct it.

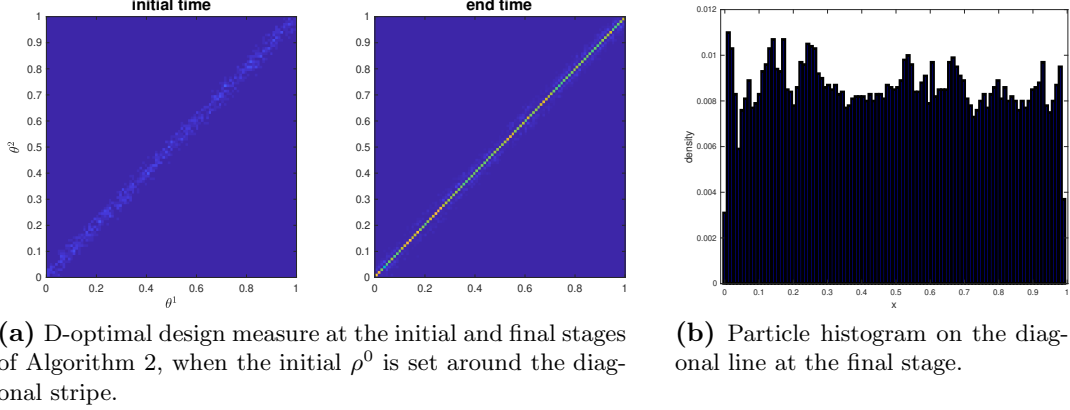


Figure 24: D-optimal warm-start case.

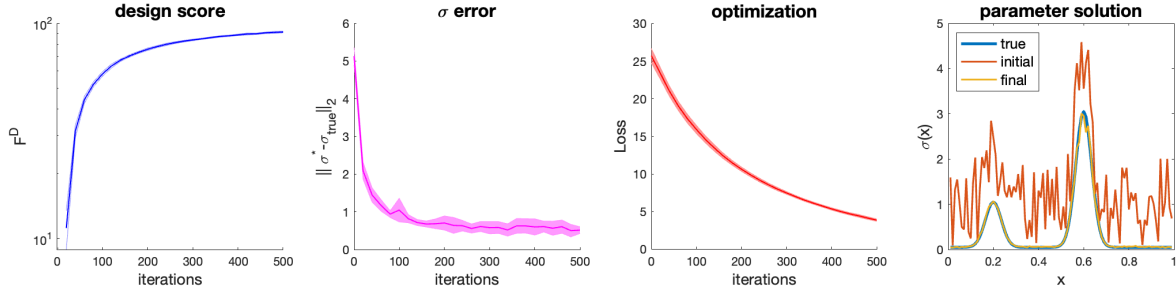


Figure 25: D-optimal warm-start case: ρ^0 concentrates along the diagonal stripe. From the left, D-design score (14b) increases and the other two error metrics decay in time. The rightmost panel shows the reconstructed σ^* at initial and final stage of Algorithm 2, in comparison to the ground-truth.

6 Conclusions and future directions

Efficient data acquisition is crucial for learning physical systems. By computing a probability distribution that quantifies the data importance, we are able to reduce the experiment cost and fetch only the valuable measurements. The novel gradient flow and particle simulation help carry out the computation for optimal design over probability measure space \mathbf{Pr}_2 . Since most physical models are highly nonlinear, the design measure ρ and the parameters to-be-reconstruct σ^* have mutual dependences. We proposed the two-layer optimization scheme that adaptively solves ρ and σ^* . We provided both the brute-force and the streamlined algorithms. Their difference lies in the update of unknowns σ for given ρ . The streamlined formulation allows the straightforward one-step update for σ , which greatly improves the computational cost. The main algorithms were applied to the Lorenz dynamical system and the Schrödinger model. Our algorithms return the design measures that identify the valuable measurements, revealing the interesting physics underneath.

Despite the promising empirical performances, the current work still has several limitations, which we leave to the future studies below.

1. **Convergence theory.** We would like to continue the theoretical aspect of the adaptive

gradient flow Algorithm 2. Open problems include the algorithm’s basic convergence rate with respect to, such as the sample size N and number of iterations T . But the mutual dependence between the design distribution ρ and the reconstruction $\sigma^*[\rho]$ prompts analytical challenges. Is it possible to examine the convergence of Algorithm 2 via studying the coupled updating system of ρ and σ^* ? Is it guaranteed that the evolution of ρ leads to the evolution of $\sigma^*[\rho]$ approaching the ground-truth σ_{true} ?

2. **Efficiency improvement.** Some hyperparameters in our algorithms (such as the sample size N) are set a priori. For computation efficiency, these hyperparameters can be tuned adaptively as well. For instance, when the sample particle θ_i gets updated, the algorithm moves on and throw away $\text{data}(\theta_i)$. Since querying the data observation consumes time and human labor, can we develop a scheme to recycle the acquired information? Can we also robustly choose the step-size Δt and iteration number T to achieve fast convergence?

References

- [1] Alen Alexanderian. Optimal experimental design for infinite-dimensional bayesian inverse problems governed by pdes: A review. *Inverse Problems*, 37(4):043001, 2021.
- [2] Alen Alexanderian, Noemi Petra, Georg Stadler, and Omar Ghattas. A-optimal design of experiments for infinite-dimensional bayesian linear inverse problems with regularized ℓ_0 -sparsification. *SIAM Journal on Scientific Computing*, 36(5):A2122–A2148, 2014.
- [3] Alen Alexanderian, Noemi Petra, Georg Stadler, and Omar Ghattas. A fast and scalable method for a-optimal design of experiments for infinite-dimensional bayesian nonlinear inverse problems. *SIAM Journal on Scientific Computing*, 38(1):A243–A272, 2016.
- [4] Alen Alexanderian and Arvind K Saibaba. Efficient d-optimal design of experiments for infinite-dimensional bayesian linear inverse problems. *SIAM Journal on Scientific Computing*, 40(5):A2956–A2985, 2018.
- [5] Luigi Ambrosio, Nicola Gigli, and Giuseppe Savaré. *Gradient flows: in metric spaces and in the space of probability measures*. Springer Science & Business Media, 2005.
- [6] Jasbir Singh Arora. *Introduction to optimum design*. Elsevier, 2004.
- [7] Jordan Ash, Surbhi Goel, Akshay Krishnamurthy, and Sham Kakade. Gone fishing: Neural active learning with fisher embeddings. In *Advances in Neural Information Processing Systems*, volume 34, pages 8927–8939. Curran Associates, Inc., 2021.
- [8] Ahmed Attia, Alen Alexanderian, and Arvind K Saibaba. Goal-oriented optimal design of experiments for large-scale bayesian linear inverse problems. *Inverse Problems*, 34(9):095009, 2018.
- [9] Corwin L Atwood. Optimal and efficient designs of experiments. *The Annals of Mathematical Statistics*, pages 1570–1602, 1969.
- [10] Ruzena Bajcsy. Active perception. *Proceedings of the IEEE*, 76(8):966–1005, 1988.

- [11] Irene Bauer, Hans Georg Bock, Stefan Körkel, and Johannes P. Schlöder. Numerical methods for optimum experimental design in dae systems. *Journal of Computational and Applied Mathematics*, 120(1):1–25, 2000.
- [12] Frank Bretz, Holger Dette, and Jose C Pinheiro. Practical considerations for optimal designs in clinical dose finding studies. *Statistics in medicine*, 29(7-8):731–742, 2010.
- [13] Rui M Castro and Robert D Nowak. Minimax bounds for active learning. *IEEE Transactions on Information Theory*, 54(5):2339–2353, 2008.
- [14] Kathryn Chaloner and Isabella Verdinelli. Bayesian Experimental Design: A Review. *Statistical Science*, 10(3):273 – 304, 1995.
- [15] Kamalika Chaudhuri, Sham M Kakade, Praneeth Netrapalli, and Sujay Sanghavi. Convergence rates of active learning for maximum likelihood estimation. *Advances in Neural Information Processing Systems*, 28, 2015.
- [16] Gaoming Chen, Fadil Santosa, and Aseel Titi. Determination of a small elliptical anomaly in electrical impedance tomography using minimal measurements. *arXiv preprint arXiv:2403.11365*, 2024.
- [17] M.A. Clyde. Experimental design: Bayesian designs. In *International Encyclopedia of the Social & Behavioral Sciences*, pages 5075–5081. Pergamon, Oxford, 2001.
- [18] Valerii Fedorov and Sergei Leonov. *Optimal Design for Nonlinear Response Models*. 07 2013.
- [19] Valerii V Fedorov and Peter Hackl. *Model-oriented design of experiments*, volume 125. Springer Science & Business Media, 2012.
- [20] Valerii Vadimovich Fedorov. *Theory of optimal experiments*. Elsevier, 2013.
- [21] A. Figalli and F. Glaudo. *An Invitation to Optimal Transport, Wasserstein Distances, and Gradient Flows*. EMS textbooks in mathematics. European Mathematical Society, 2021.
- [22] Adam Foster, Martin Jankowiak, Matthew O’Meara, Yee Whye Teh, and Tom Rainforth. A unified stochastic gradient approach to designing bayesian-optimal experiments. In *International Conference on Artificial Intelligence and Statistics*, pages 2959–2969. PMLR, 2020.
- [23] Yarin Gal, Riashat Islam, and Zoubin Ghahramani. Deep Bayesian active learning with image data. In Doina Precup and Yee Whye Teh, editors, *Proceedings of the 34th International Conference on Machine Learning*, volume 70 of *Proceedings of Machine Learning Research*, pages 1183–1192. PMLR, 06–11 Aug 2017.
- [24] Daniel Golovin, Andreas Krause, and Debajyoti Ray. Near-optimal bayesian active learning with noisy observations. *Advances in Neural Information Processing Systems*, 23, 2010.
- [25] David J Griffiths and Darrell F Schroeter. *Introduction to quantum mechanics*. Cambridge university press, 2018.
- [26] E Haber, L Horesh, and L Tenorio. Numerical methods for experimental design of large-scale linear ill-posed inverse problems. *Inverse Problems*, 24(5):055012, sep 2008.

- [27] E Haber, L Horesh, and L Tenorio. Numerical methods for the design of large-scale nonlinear discrete ill-posed inverse problems. *Inverse Problems*, 26(2):025002, 2009.
- [28] Eldad Haber, Zhuojun Magnant, Christian Lucero, and Luis Tenorio. Numerical methods for α -optimal designs with a sparsity constraint for ill-posed inverse problems. *Computational Optimization and Applications*, 52:293–314, 2012.
- [29] Linda M Haines, Inna Perevozskaya, and William F Rosenberger. Bayesian optimal designs for phase i clinical trials. *Biometrics*, 59(3):591–600, 2003.
- [30] Michael Hinze, René Pinnau, Michael Ulbrich, and Stefan Ulbrich. *Optimization with PDE Constraints*, volume 23. Springer Science & Business Media, 2008.
- [31] Neil Houlsby, Ferenc Huszár, Zoubin Ghahramani, and Máté Lengyel. Bayesian active learning for classification and preference learning. *arXiv preprint arXiv:1112.5745*, 2011.
- [32] Xun Huan, Jayanth Jagalur, and Youssef Marzouk. Optimal experimental design: Formulations and computations. *Acta Numerica*, 33:715–840, 2024.
- [33] Xun Huan and Youssef M Marzouk. Simulation-based optimal bayesian experimental design for nonlinear systems. *Journal of Computational Physics*, 232(1):288–317, 2013.
- [34] Xun Huan and Youssef M Marzouk. Gradient-based stochastic optimization methods in bayesian experimental design. *International Journal for Uncertainty Quantification*, 4(6), 2014.
- [35] Xun Huan and Youssef M Marzouk. Sequential bayesian optimal experimental design via approximate dynamic programming. *arXiv preprint arXiv:1604.08320*, 2016.
- [36] Jayanth Jagalur-Mohan and Youssef Marzouk. Batch greedy maximization of non-submodular functions: Guarantees and applications to experimental design. *The Journal of Machine Learning Research*, 22(1):11397–11458, 2021.
- [37] Ruhui Jin, Martin Guerra, Qin Li, and Stephen Wright. Optimal experimental design for linear models via gradient flow. *arXiv preprint arXiv:2401.07806*, 2024.
- [38] Ming-Hung Kao and Hazar Khogeer. Optimal designs for mixed continuous and binary responses with quantitative and qualitative factors. *Journal of Multivariate Analysis*, 182:104712, 2021.
- [39] J. Kiefer. General Equivalence Theory for Optimum Designs (Approximate Theory). *The Annals of Statistics*, 2(5):849 – 879, 1974.
- [40] J. Kiefer and J. Wolfowitz. Optimum Designs in Regression Problems. *The Annals of Mathematical Statistics*, 30(2):271 – 294, 1959.
- [41] Andreas Kirsch. An introduction to the mathematical theory of inverse problems. *Applied Mathematical Sciences*, 1996.
- [42] Steven George Krantz and Harold R Parks. *The implicit function theorem: history, theory, and applications*. Springer Science & Business Media, 2002.

- [43] Fengyi Li, Ayoub Belhadji, and Youssef Marzouk. Nonlinear bayesian optimal experimental design using logarithmic sobolev inequalities. *arXiv preprint arXiv:2402.15053*, 2024.
- [44] Edward N. Lorenz. Deterministic nonperiodic flow. *Journal of Atmospheric Sciences*, 20(2):130 – 141, 1963.
- [45] Alexander I Lvovsky and Michael G Raymer. Continuous-variable optical quantum-state tomography. *Reviews of modern physics*, 81(1):299–332, 2009.
- [46] Toby J. Mitchell. An algorithm for the construction of “D-optimal” experimental designs. *Technometrics*, 42(1):48–54, 2000.
- [47] Stephen Mussmann, Julia Reisler, Daniel Tsai, Ehsan Mousavi, Shayne O’Brien, and Moises Goldszmidt. Active learning with expected error reduction. *arXiv preprint arXiv:2211.09283*, 2022.
- [48] Friedrich Pukelsheim. *Optimal Design of Experiments*. Society for Industrial and Applied Mathematics, 2006.
- [49] Jerome Sacks, William J Welch, Toby J Mitchell, and Henry P Wynn. Design and analysis of computer experiments. *Statistical Science*, 4(4):409–423, 1989.
- [50] Filippo Santambrogio. *Optimal Transport for Applied Mathematicians: Calculus of Variations, PDEs, and Modeling*, volume 87. Birkhäuser, 2015.
- [51] Fadil Santosa and Loren Anderson. Bayesian sequential optimal experimental design for linear regression with reinforcement learning. In *2022 21st IEEE International Conference on Machine Learning and Applications (ICMLA)*, pages 641–646, 2022.
- [52] Ozan Sener and Silvio Savarese. Active learning for convolutional neural networks: A core-set approach. *arXiv preprint arXiv:1708.00489*, 2017.
- [53] Burr Settles. Active learning literature survey. 2009.
- [54] Albert Tarantola. *Inverse problem theory and methods for model parameter estimation*. SIAM, 2005.
- [55] Henry P Wynn. The sequential generation of d -optimum experimental designs. *The Annals of Mathematical Statistics*, 41(5):1655–1664, 1970.
- [56] Barton Zwiebach. *Mastering quantum mechanics: essentials, theory, and applications*. MIT Press, 2022.